

## **The Effect of Clay Type on the Properties of Cohesive Sediment Gravity Flows and their Deposits**

Baker, Megan L.; Baas, Jaco H.; Malarkey, Jonathan; Silva Jacinto, Ricardo; Craig, Melissa J.; Kane, Ian A.; Barker, Simon

**Journal of Sedimentary Research**

DOI:  
[10.2110/jsr.2017.63](https://doi.org/10.2110/jsr.2017.63)

Published: 01/01/2017

Peer reviewed version

[Cyswllt i'r cyhoeddiad / Link to publication](#)

*Dyfyniad o'r fersiwn a gyhoeddwyd / Citation for published version (APA):*  
Baker, M. L., Baas, J. H., Malarkey, J., Silva Jacinto, R., Craig, M. J., Kane, I. A., & Barker, S. (2017). The Effect of Clay Type on the Properties of Cohesive Sediment Gravity Flows and their Deposits. *Journal of Sedimentary Research*, 87(11), 1176-1195.  
<https://doi.org/10.2110/jsr.2017.63>

### **Hawliau Cyffredinol / General rights**

Copyright and moral rights for the publications made accessible in the public portal are retained by the authors and/or other copyright owners and it is a condition of accessing publications that users recognise and abide by the legal requirements associated with these rights.

- Users may download and print one copy of any publication from the public portal for the purpose of private study or research.
- You may not further distribute the material or use it for any profit-making activity or commercial gain
- You may freely distribute the URL identifying the publication in the public portal ?

### **Take down policy**

If you believe that this document breaches copyright please contact us providing details, and we will remove access to the work immediately and investigate your claim.

**THE EFFECT OF CLAY TYPE ON THE PROPERTIES OF COHESIVE  
SEDIMENT GRAVITY FLOWS AND THEIR DEPOSITS**

**MEGAN L. BAKER<sup>1</sup>**  
**JACO H. BAAS<sup>1</sup>**  
**JONATHAN MALARKEY<sup>1</sup>**  
**RICARDO SILVA JACINTO<sup>2</sup>**  
**MELISSA J. CRAIG<sup>3</sup>**  
**IAN A. KANE<sup>4</sup>**  
**SIMON BARKER<sup>5</sup>**

<sup>1</sup> School of Ocean Sciences, Bangor University, Menai Bridge, Anglesey, LL59 5AB, U.K.

<sup>2</sup> IFREMER, Laboratoire Géodynamique et Enregistrement Sédimentaire (LGS), BP70, 29280  
Plouzané, France

<sup>3</sup> Australian School of Petroleum, University of Adelaide, Adelaide, SA 5005, Australia

<sup>4</sup> School of Earth and Environmental Sciences, The University of Manchester, Oxford Road,  
Manchester, M13 9PL, U.K.

<sup>5</sup> Statoil ASA, Research Centre Bergen, NO-5020 Bergen, Norway

Corresponding author: m.baker@bangor.ac.uk

Running head: EFFECT OF CLAY TYPE ON COHESIVE SEDIMENT GRAVITY FLOWS

Key Words: Clay, Flume, Sediment Gravity Flow, Cohesion, Yield Stress

## ABSTRACT

The present knowledge of cohesive clay-laden sediment gravity flows (SGFs) and their deposits is limited, despite clay being one of the most abundant sediment types on earth and subaqueous SGFs transporting large volumes of sediment into the ocean. Lock-exchange experiments were conducted to contrast SGFs laden with non-cohesive silica flour, weakly cohesive kaolinite, and strongly cohesive bentonite in terms of flow behavior, head velocity, run-out distance, and deposit geometry across a wide range of suspended sediment concentrations.

The three sediment types shared similar trends in the types of flows they developed, the maximum head velocity of the flows, and the deposit shape. As suspended sediment concentration was increased, the flow type changed from low-density turbidity current (LDTTC) via high-density turbidity current (HDTTC) and mud flow to slide. As a function of increasing flow density the maximum head velocity of LDTTCs and relatively dilute HDTTCs increased, whereas the maximum head velocity of the mud flows, slides, and relatively dense HDTTCs decreased. The increase in maximum head velocity was driven by turbulent support of the suspended sediment and the density difference between the flow and the ambient fluid. The decrease in maximum head velocity comprised attenuation of turbulence by grain-to-grain frictional forces within the silica flour flows and by pervasive cohesive forces within the kaolinite and bentonite flows. The silica flour flows changed from turbulence-driven to friction-driven at a volumetric concentration of 47% and a maximum head velocity of  $0.75 \text{ m s}^{-1}$ ; the thresholds between turbulence-driven to cohesion-driven flow for kaolinite and bentonite were 22% and  $0.50 \text{ m s}^{-1}$ , and 16% and  $0.37 \text{ m s}^{-1}$ , respectively. The HDTTCs produced deposits that were wedge-shaped with a block-shaped downflow extension, the mud flows produced wedge-shaped deposits with partly or fully detached outrunner blocks, and the slides produced wedge-shaped deposits without extension. For the mud flows, slides, and most HDTTCs, an increasingly higher concentration was needed to produce similar maximum head velocities and run-out distances for flows carrying bentonite, kaolinite and silica flour, respectively. The strongly cohesive bentonite flows were able to create a stronger network of particle bonds than the weakly cohesive kaolinite flows of similar concentration. The silica flour flows remained mobile up to an extremely high concentration of 52%, and frictional forces were only able to counteract the excess density of the flows, and attenuate the turbulence within these flows, at concentrations above 47%.

Dimensional analysis of the experimental data shows that the yield stress of the pre-failure suspension can be used to predict the run-out distance and the dimensionless head velocity of the SGFs, independent of clay type. Extrapolation to the natural environment suggests that high-density SGFs laden with weakly cohesive clay reach a greater distance from their origin than flows that carry

54 strongly cohesive clay at a similar suspended sediment concentration, whilst equivalent fine-grained,  
55 non-cohesive SGFs travel the furthest. The contrasting behavior of fine-grained SGFs laden with  
56 different clay minerals may extend to differences in architecture of large-scale sediment bodies  
57 within deep marine systems.

## INTRODUCTION

Sediment gravity flows (SGF) are produced when gravity acts on the density difference between two fluids, and the excess density is provided by suspended sediment (Middleton and Hampton 1973; Kneller and Buckee 2000). Subaqueous SGFs are volumetrically one of the most important sediment transport processes on our planet, providing large quantities of sediment to lakes, seas and oceans (*e.g.*, Kneller and Buckee 2000; Talling et al. 2015). As a result of their unpredictability and often large magnitude, SGFs can pose a significant threat to engineering works in deep water, such as drilling rigs and communication cables (Baas 2005). The deposits of these flows produce submarine fans, which are amongst the largest sedimentary bodies on Earth, and store the world's greatest reserves of oil and gas (Middleton 1993; Kneller and Buckee 2000; Baas 2005; Keevil et al. 2006). Much of what is known about SGFs originates from investigations in laboratory flumes (*e.g.*, Sumner et al. 2009; de Leeuw et al. 2016), where controlled experiments provide a powerful method for understanding the flow dynamics. These laboratory studies complement descriptive core and outcrop studies, and state-of-the-art direct monitoring (Xu 2011; Sumner and Paull 2014; Xu et al. 2014). The majority of laboratory experiments have focused on sand-rich, non-cohesive, SGFs (*e.g.*, Kuenen 1951; Parker et al. 1987; Middleton and Neal 1989; Baas et al. 2005), despite the fact that cohesive mud, made up of silt- and clay-sized particles, is the most abundant sediment type on the Earth surface (Hillier 1995; Healy et al. 2002; Schindler et al. 2015). It is therefore likely that mud is common within SGFs in the natural environment. Many examples of muddy, cohesive, SGFs exist in the modern environment, such as at the mouth of the Zaire river in west-central Africa (Heezen et al. 1964; van Weering and van Ipereren 1984; Droz et al. 2003), and in the ancient environment, such as in the Cretaceous Britannia Sandstone Member, North Sea (Barker et al. 2008), and in the Silurian Aberystwyth Grits of Cardigan Bay, Wales (Wilson et al. 1992; Talling et al. 2004).

Cohesive SGFs are more complex than their non-cohesive counterparts, because of the unique ability of suspended clay minerals to form flocs and gels (Winterwerp and van Kesteren 2004). Flocs are aggregates composed of clay particles that bind together when the attractive Van der Waals forces outcompete repulsive forces between the negatively charged surface of clay particles, often aided by the presence of positively charged ions in the water (Winterwerp and van Kesteren 2004). The presence of flocs within the flow increases the viscosity and yield stress of the flow and may thus affect the turbulence driving the flow (Baas and Best 2002). The amount of flocculation and the size of the flocs generally increase as the bulk suspended clay concentration increases (Baas et al. 2009). Eventually, a "gelling" point may be reached at high clay concentration, which is characterized by the formation of a volume-filling network of particle bonds in the liquid (Blackbourn and Thompson, 2000; Low and Guy, 2000; Baas et al. 2009). A stable gel of linked clay minerals may be

92 viscous enough to cause the total suppression of turbulence within the flow. Conversely, the  
93 electrostatic bonds between the clay particles can be broken in regions of high shear. Thus, an  
94 increase in turbulence generation within the flows by, for example, an increasing slope gradient has  
95 the potential to break up bonds between clay particles, and reduce the flow viscosity and yield  
96 stress. This constantly shifting balance between turbulent and cohesive forces regulates the dynamic  
97 structure of cohesive SGFs (Baas et al. 2009).

98 The cohesive forces within a clay flow, and hence its rheology, have been shown to change with clay  
99 concentration (Baas and Best 2002; Felix and Peakall 2006; Baas et al. 2009; Sumner et al. 2009), but  
100 the type of clay mineral can also change the cohesive properties of the flow (Marr et al. 2001; Baas  
101 et al. 2016). Different clay minerals have different shapes, sizes, layer charges, cation exchange  
102 capacities (CEC), edge charge densities, and structures of the particle edges, all of which control the  
103 rheological and cohesive properties of the clay flow (Lagaly 1989). It is important to note that some  
104 of these properties are also controlled by pH and the available ions in the medium (Luckham and  
105 Rossi 1999), which may vary independently of clay mineral type.

106 The common clay minerals kaolinite and bentonite have been considered to be end members in  
107 terms of cohesive properties, where kaolinite is weakly cohesive and bentonite is strongly cohesive.  
108 This can largely be explained by their different chemical and physical properties (Table 1). Kaolinite  
109 particles are relatively large and have a low specific surface area (SSA), which is the ratio of surface  
110 area of a material to either its volume or mass (Table 1; Holtz and Kovacs 1981; Yong et al. 2012).  
111 The surface area of the particle controls the magnitude of the interparticle forces, with a larger SSA  
112 allowing greater interparticle forces (Atkinson 2007). Bentonite particles are relatively small and  
113 have a large SSA, which is further increased by the ability of bentonite to absorb water into its  
114 chemical structure. These water molecules separate unit layers within the clay mineral, causing it to  
115 expand, or swell, and thus increase the particle surface area (Yong et al. 2012). The cation exchange  
116 capacity (CEC) is a measure of the potential chemical activity of a clay mineral. Cohesive forces are  
117 directly related to the chemical activity of a clay, and thus to the CEC (Kooistra et al. 1998; Khabbazi  
118 Basmenj et al. 2016). The high CEC of bentonite compared to kaolinite further explains its greater  
119 cohesive properties. Illite and chlorite are clay minerals with intermediate cohesive properties (Table  
120 1), also commonly found in natural sediment. Illite and montmorillonite (which includes bentonite)  
121 have been found to be the most abundant clay minerals on the modern seafloor, each accounting  
122 for roughly 35% of the clay size fraction. Chlorite and kaolinite are less abundant, both accounting  
123 for approximately 15% of the clay size fraction (Griffin et al. 1968; Windom, 1976; Hillier, 1995).

Investigations of the effect of clay type on the dynamics of SGFs and their depositional properties began recently. Marr et al. (2001) conducted an experimental study of the flow mechanics of sand-rich subaqueous gravity flows, which also carried bentonite or kaolinite clay, and found that 0.7% by weight of bentonite was sufficient to produce coherent flows, compared with 7% by weight for kaolinite. Marr et al. (2001) defined coherent flows as flows that resist breaking apart and becoming completely turbulent under the dynamic stress associated with the head of a propagating debris flow. The lower threshold concentration of bentonite required to produce a coherent gravity flows was attributed to the higher yield stress of bentonite mixtures compared to kaolinite mixtures of the same composition. Baas et al. (2016) found experimentally that the volumetric suspended sediment concentration needed to produce transitional flow behavior (*sensu* Baas and Best 2002) is much lower in bentonite flows than in kaolinite flows. This was attributed to the greater cohesive strength of bentonite, producing flows with a significantly higher molecular viscosity and yield stress than kaolinite flows at concentrations above the gelling threshold.

In the present paper, further experimental evidence that clay type is an important control on cohesive sediment gravity flows is provided. These experiments produced flows over a wide range of suspended sediment concentrations to produce low-density turbidity currents, high-density turbidity currents, debris flows, and slides. The principal aims of this research included:

1. To determine how clay concentration and clay type qualitatively affect the flow properties and quantitatively affect the flow velocity, run-out distance, and deposit geometry of fine-grained SGFs produced in the laboratory.
2. To investigate if the rheological properties of the pre-failure suspensions can be used to predict the flow velocity and run-out distance of the laboratory SGFs, independent of clay type and concentration.
3. To discuss the possible implications of the experimental data for natural SGFs and their deposits.

## METHODS

Thirty-two laboratory experiments were conducted in a smooth-bottomed lock-exchange flume, 5 m long, 0.2 m wide and 0.5 m deep (Fig. 1). The experiments were conducted using seawater from the Menai Strait (NW Wales, U.K.) to better mimic flows in the deep ocean. Seawater contains a larger number of cations compared to freshwater, which helps reduce the repulsive forces between the negatively charged clay particles and enhance flocculation (Tan et al. 2014). In each experiment, the slope of the flume was set to 0°, and the reservoir was filled with a suspension of fine sediment and seawater, separated by a lock gate from the main compartment of the flume that was filled with ambient seawater (density  $\rho_a = 1.027 \text{ g cm}^{-3}$ ). The lock gate was then lifted to initiate the sediment

gravity flow. The experimental program comprised three different sediment types of contrasting rheological properties: (1) mixtures of non-cohesive silica flour ( $D_{50} = 18.2 \mu\text{m}$ , density  $\rho_s = 2650 \text{ kg m}^{-3}$ ) and seawater, comprising initial volumetric sediment concentrations,  $C$ , of 1% to 52%; (2) weakly cohesive kaolinite-seawater ( $D_{50} = 9.1 \mu\text{m}$ ,  $\rho_s = 2600 \text{ kg m}^{-3}$ ) mixtures, ranging from  $C = 1\%$  to  $C = 29\%$ , and; (3) strongly cohesive bentonite-seawater ( $D_{50} = 5.6 \mu\text{m}$ ,  $\rho_s = 2300 \text{ kg m}^{-3}$ ) mixtures, with  $C$ -values between 1% and 20% (Table 2). These experiments examined the changes in behavior of the sediment gravity flows as a function of suspended sediment concentration and sediment type. In order to anticipate possible time-dependent behavior, a consistent method was used to prepare each suspension. First, half of the seawater and the sediment were combined and mixed in a cement mixer for 15 minutes. The remaining seawater and sediment was then added and mixed for a further 15 minutes. Subsequently, the mixture was decanted into a container and further mixed by a handheld mixer for 3 minutes for kaolinite and silica flour and for 10 minutes for bentonite, to obtain a lump-free suspension. The suspension was then progressively added to the reservoir while the flume filled with seawater, in order to keep similar fluid levels on each side of the lock gate to limit pressure on the gate. Each flow was generated from the same volume and depth of mixture into a body of seawater of the same depth ( $h = 0.35 \text{ m}$ ). The suspension within the reservoir was mixed using the handheld mixer for 60 s immediately prior to lifting the gate and generating the sediment gravity flow.

A time-series of the head velocity of each sediment gravity flow was obtained from the footage of a high-definition video camera that tracked the front of the flow along the length of the tank. The change in head position between the video frames was measured based on the distance moved in pixels relative to a scale at the bottom of the flume, and velocity was then calculated using the timestamp of each frame. The morphology of the deposits of the SGFs was measured along the center line of the flume using a SeaTek 5 MHz Ultrasonic Ranging System, comprised of 16 transducers that were spaced apart by 16.2 mm. The SeaTek ranging system calculates the vertical distance to the deposit by means of the two-way travel time of an ultrasound pulse. The housing array of the transducers was arranged parallel to the direction of flow and was moved 0.122 m downstream between individual readings, thus producing a profile with a data point every 8.1 mm along the deposit. A blank scan of the bottom of the flume was subtracted from the bed profile to determine deposit thicknesses. The run-out distance of each deposit (defined as the distance from the lock gate) was recorded for all flows that stopped before reaching the end of the flume. A hypothetical run-out distance was determined for the flows that bounced off the far end of the flume, as explained in Section 5.1.2.

The rheological characteristics of sediment mixtures with the same composition as the suspensions used in the lock-exchange experiments were measured using the Anton Paar Physica MCR 301 rheometer at IFREMER (Brest, France). These experiments were carried out at 20°C and used a concentric cylinder geometry. The tests were conducted on kaolinite suspensions at concentrations ranging from  $C = 5\%$  to  $C = 29\%$  and on bentonite suspensions ranging from  $C = 5\%$  to  $C = 20\%$ . Each experiment used 200 cm<sup>2</sup> samples, prepared by weighing seawater from the Menai Strait and clay within a plastic bottle at the desired concentration. The bottle was then manually shaken for 10 minutes to produce a homogenous suspension. The sample was shaken for an additional 30 seconds immediately before a subsample of the suspension was added to the rheometer cup to account for any settling that may have taken place at low clay concentrations. Time-dependency tests on the rheological parameters were conducted and found to be insignificant within the time frame of the experimental method. The rheometer measured the rheological behavior of the suspensions, from which the yield stress (or critical shear stress) was derived to give an approximation of the strength of the cohesive bonds between the clay particles. Yield stress values obtained from the oscillatory test are presented in Table 2. This method applies a progressively increasing oscillating strain to the sediment and measures the resultant stress (van Vliet 2013). The trend between yield stress and clay concentration derived from the oscillatory tests was found to agree well with that of strain- and stress-controlled tests also conducted for both clay types.

## EXPERIMENTAL RESULTS

Each experiment produced a sediment gravity flow directly after lifting the gate. The flow behavior was observed to vary with the initial suspended sediment concentration and the type of sediment. Below, differences in the shape and kinematic behavior of the head of the flows, and spatial trends in the head velocities and deposit thicknesses of the flows, are described for the non-cohesive silica flour (Figs 2-4), the weakly cohesive kaolinite (Figs 5-7), and the strongly cohesive bentonite (Figs 8-10). Table 2 summarizes the sediment type, the flow type, the initial suspended sediment concentration, the initial yield stress, the maximum head velocity for each flow, and the run-out distance for each deposit. The results for the non-cohesive silica-flour laden flows and the cohesive flows laden with kaolinite and bentonite are described below first. The differences in flow behavior and deposit properties for these sediment types are then captured in an empirical model for the effect of cohesion on the kinematic behavior of fine-grained sediment gravity flows.

### *Silica flour flows*

**Visual observations.**--- Video recordings of the silica-flour laden flows show marked changes in the behavior of the heads of these flows, as the initial suspended sediment concentration,  $C$ , was

increased from 1% to 52%. Along the entire length of the flume, the flows that carried up to 44% silica flour were visually dominated by turbulent mixing, both within the head and body of the flows, and at their boundaries (Figs 2A, B). Upon leaving the reservoir, these flows developed a pointed semi-elliptically shaped head with a prominent nose. This shape, as well as the thickness of the head of these flows, remained constant along the flume. The height of the body fluctuated owing to the development of Kelvin-Helmholtz instabilities at the upper surface of the flows.

The flows that carried between 46% and 50% silica flour comprised two layers: a lower layer without visible internal mixing and an upper layer where ambient water was mixed into the flow (Fig. 2C). The boundary between these two layers was well defined in the videos by a vertical change in color (Fig. 2C). This color contrast increased from  $C = 46\%$  to  $C = 50\%$ . The heads of the 46% to 48% silica flour flows showed a semi-elliptical shape similar to the  $C < 46\%$  flows. However, the nose gradually became more rounded, as the concentration increased. At  $C \geq 49\%$ , the shape of the head of the silica-flour laden flows was rounded with a blunter nose than at lower  $C$ -values. At  $C \geq 47\%$ , the flows stopped before reaching the end of the tank, but sediment from the dilute upper layer of the flow continued to travel along the length of the flume.

The  $C = 51\%$  and  $C = 52\%$  flows were poorly mixed internally and exhibited only minor incorporation of ambient water (Fig. 2D). Instead, the ambient water was swept over the front and the top of the flows. The 52% flow was wedge-shaped, rendering it difficult to distinguish the head from the body of this flow. A dilute cloud of silica flour developed above the flows with  $C = 51\%$  and  $C = 52\%$  (Fig. 2D). This cloud travelled slowly down the length of the flume after the main flow had stopped.

**Flow velocities.**--- Figures 3A and 3B show distinct spatial changes in the head velocity of the flows, as the silica flour concentration was increased. Each flow accelerated rapidly once the gate was lifted, reaching a maximum head velocity that increased from  $0.11 \text{ m s}^{-1}$  to  $0.75 \text{ m s}^{-1}$ , as the suspended sediment concentration of the flows was increased from 1% to 47%. At  $C \geq 48\%$ , the maximum head velocity of the flows decreased progressively from  $0.71 \text{ m s}^{-1}$  to  $0.29 \text{ m s}^{-1}$  (Fig. 11A). After the initial increase in head velocity, all flows decelerated along the remainder of the flow path. However, higher-frequency fluctuations in the head velocity were superimposed on this trend of decelerating head velocity, especially in the denser flows. The maximum recorded fluctuation in head velocity was c.  $0.2 \text{ m s}^{-1}$  in the 46% flow (Fig. 3B). Within the limits of the flume, the flows with  $C \leq 25\%$  showed a gradual spatial decrease in head velocity, while the  $C = 40\%$  to  $C = 46\%$  flows exhibited a quicker rate of deceleration in the final flow stages, in addition to this gradual decrease. The flows with  $C \geq 47\%$  flows also displayed a rapid decrease in velocity in the final stages of flow, but for these flows, the velocity reduced to zero before reaching the far end of the flume. As the

initial silica flour concentration was increased from 47% to 52%, the maximum distance of travel of these flows progressively shortened (Figs 3B, 11B).

**Deposits.**--- All the flows with  $C \geq 47\%$  produced a measurable run-out distance (Fig. 4), translating into deposit lengths that decreased from 4.66 m to 0.49 m, as the initial suspended sediment concentration of the flows was increased from 47% to 52% (Fig. 11B). These deposits were thickest at the back of the reservoir, where also the maximum thickness increased with increasing flow density (Fig. 4). The deposits of the 47% to 49% flows decreased steadily in thickness from the back of the reservoir to  $x \approx 1.1$  m; thereafter, the thickness of these deposits remained constant. The termination of the deposit of the 47% flow was wedge-shaped, whereas the deposits of the 48% and 49% flows had abrupt terminations (Fig. 4). The 50% and 51% flows produced deposits that thinned from the back of the reservoir to  $x = 0.83$  m and  $x = 0.65$  m, respectively, before increasing in thickness again, thus exhibiting a distinct depression within the deposits. As with the 48% and 49% flows, the deposits of the 50% and 51% flows terminated abruptly. The flow that carried 52% silica flour did not produce a depression within its deposit. Instead, this deposit dipped steeply and almost uniformly from the back of the reservoir to  $x = 0.49$  m (Fig. 4).

#### *Kaolinite flows*

**Visual observations.**--- The behavior of the heads of the flows laden with kaolinite clay changed significantly, as the suspended sediment concentration was increased from 1% to 29%. The 1% to 15% flows were all turbulent, behaving in a similar manner to the low-concentration silica flour flows (Fig. 2A). As the initial concentration was increased from 1% to 15%, turbulent mixing within the flows and mixing with the ambient water at the flow boundaries was observed to intensify. These kaolinite flows produced pointed semi-elliptically shaped heads with a pronounced nose; this shape remained constant along the full extent of the flow path. The upper boundary of the body of these flows contained Kelvin-Helmholtz waves and instabilities.

The  $C = 22\%$  to  $C = 25\%$  flows comprised a dark lower layer, overlain by an upper layer with a lighter shade, where ambient water mixed into the flow (Figs 5A, B). Fluid escape structures (FES) developed within the lower layer of the 22% and 23% flows, at 1.32 m and 0.84 m along the length of the tank, respectively; these FES were maintained until the final flow stages. The majority of the FES were angled at  $40^\circ$  relative to the horizontal in the 22% flow; this angle was  $10^\circ$  in the 23% flow. From 1.32 m, the head of the  $C = 22\%$  flow was visually divided into three parts (Fig. 5A): a featureless basal zone 1a, a middle zone 1b with the angled FES, and an upper zone 2 where mixing with ambient water dominated. This tripartite structure was visible until 3.30 m, after which the FES ceased to exist. The heads of the  $22\% \leq C \leq 25\%$  kaolinite flows had a pointed semi-elliptical shape

with a prominent nose, and all experienced hydroplaning. However, from 0.41 m to 1.35 m from the point of release, the shape of the head of the 25% flow changed to a rounded semi-ellipse, as sediment was thrown over the top of the head (Fig. 5B).

The pointed, wedged-shaped head of the 27% kaolinite flow lacked evidence of internal turbulent mixing, and mixing with the ambient fluid along the flow path was weak at best (Fig. 5C). The head of this flow hydroplaned, and it developed vertical tension cracks ( $< 10$  mm deep) oriented perpendicular to the side wall of the flume. The 29% kaolinite suspension slid out of the reservoir as a coherent mass, producing a flow with a blunt, rounded head and a steeply inclined body (Fig. 5D). Mixing with the ambient water and hydroplaning was absent at  $C = 29\%$ .

**Flow velocities.**--- Figures 6A and 6B reveal distinct changes in head velocity as a function of distance along the flume, as the suspended kaolinite concentration was increased from 1% to 29%. All kaolinite flows accelerated upon leaving the reservoir, before gradually decelerating, as they travelled further down the flume (Fig. 6). Hence, all flows reached a maximum velocity, which increased from  $0.11 \text{ m s}^{-1}$  for  $C = 1\%$  to  $0.50 \text{ m s}^{-1}$  for  $C = 22\%$ , and then decreased to  $0.29 \text{ m s}^{-1}$  for  $C = 29\%$  (Fig. 11A). The rate of flow deceleration increased slightly, as the suspended sediment concentration was increased from 1% to 15%, as did short-term variations in head velocity superimposed on the long-term trend of flow deceleration, with the 15% flow fluctuating in head velocity by up to  $0.1 \text{ m s}^{-1}$  (Fig. 6A). The flows with  $C \geq 22\%$  displayed a phase of rapid deceleration immediately before coming to a halt (Fig. 6B). The 15% flow shows the beginning of a similar trend (Fig. 6A), but it did not reach zero velocity before arriving at the far end of the flume, conforming to all flows with  $C < 15\%$ . The 29% kaolinite flow behaved somewhat differently, in that, after an initial deceleration from  $0.3 \text{ m s}^{-1}$  to  $\sim 0.01 \text{ m s}^{-1}$ , the flow continued to move forward at  $0.01 \text{ m s}^{-1}$  over a distance of 0.33 m before stopping (Fig. 6B). The maximum distance that the flows with  $C \geq 22\%$  travelled decreased, as the suspended sediment concentration was increased (Figs 6B, 11B).

**Deposits.**--- The sediment gravity flows that carried 22-29% kaolinite formed deposits that were fully confined within the flume. As the suspended sediment concentration was increased from 22% to 29%, the run-out distance of the deposits decreased from 4.35 m to 0.46 m (Figs 7, 11B). Figure 7 also shows that these deposits were thickest near the back of the reservoir, and that the shape of the deposits differed profoundly. The deposits formed by the flows that carried 22-27% kaolinite terminated abruptly, thus showing beds with a pronounced leading edge. The height of this leading edge above the base of the flume increased, as the suspended sediment concentration was increased from 22% to 27% (Fig. 7). The deposits of the 22% and 23% flows thinned from the back of the reservoir to  $x \approx 0.95 \text{ m}$ , before remaining constant in thickness down to their distal termination.

In contrast, the deposits of the 25% and 27% flows both comprised a distinct depression, which reached the floor of the flume at  $x = 0.71$  m for the flow with  $C = 25\%$ , while there was 0.016 m of clay in the depression of the deposit of the 27% flow at  $x = 0.50$  m (Fig. 7). The deposit of the 29% flow progressively decreased in thickness from the back of the reservoir, thus producing a steep, wedge-shaped deposit.

#### *Bentonite flows*

**Visual observations.**--- The density flows laden with bentonite clay mimicked the flows laden with silica flour and kaolinite in that the behavior of the heads of these flows changed substantially as a function of suspended sediment concentration. At  $C \leq 10\%$ , the flows exhibited strong turbulent mixing, both internally and at their boundaries, and distinct Kelvin-Helmholtz instabilities developed at the interface with the ambient water in the body region in a similar manner to the low concentration silica flour flows (Fig. 2A). The heads of these flows had a semi-elliptical shape and a well-defined nose.

The flows with  $C = 15\%$  and  $C = 16\%$  exhibited a dense lower layer and a dilute upper layer, similar to those described above for the 22-25% kaolinite flows. Here, the two layers were separated by interfacial waves that were particularly prominent during the final flow stages of the  $C = 15\%$  flow. The lower layer of the  $C = 15\%$  flow remained featureless during the initial and final flow stages, but FES were present in the midsection of the flow path. In the 16% flow, a long quasi-horizontal FES developed at  $x \approx 0.60$  m, above which multiple FES angled at  $45^\circ$  were observed (Fig. 8A). This layer of FES moved on top of a dense, featureless layer to  $x \approx 3$  m; further down the tank, the entire dense lower layer was featureless. The video recordings revealed packets of cohesive sediment within the head of the 15% flow and more frequently within the 16% flow (Fig. 8A). Occasionally, these packets were pushed over the top of the head before disintegrating or carried along at the floor of the flume before being incorporated into the head of the flow (Fig. 8A). The head of the flow with  $C = 17\%$  had a tripartite signature: (i) a dense lower layer which contained horizontal sheets of water; (ii) a middle layer with active mixing and FES; and (iii) a dilute upper layer, dominated by mixing with the ambient water (Fig. 8B). This tripartite structure was visible from  $x = 1.05$  m to  $x = 2.43$  m, after which the FES reached the base of the flow, producing a two-partite structure. The heads of the 15% and 16% flows were semi-elliptical in shape with a well-defined nose (Fig. 8A), whereas the front of the 17% flow was more semi-circular (Fig. 8B).

Between  $C = 15\%$  and  $C = 19\%$ , the heads of all the bentonite flows showed hydroplaning. Yet, the shape of the head of the flows that carried 18% and 19% bentonite was different from that of the bentonite flows with lower  $C$ -values. Upon leaving the reservoir, the heads of these flows lifted off

the base of the flume and folded back on themselves, thus attaining a distinct and persistent roller-wave like shape (Fig. 8C). The body of the 18% and 19% flows lacked any noticeable mixing, but a dilute suspension cloud developed above the heads of these flows (Fig. 8C). During the final flow stages, the fold at the top of the head dropped back towards the floor of the flume, resulting in a blunt semi-circular frontal shape. Vertical tension cracks were observed in the body of the flow that carried 19% bentonite. The highest-concentration bentonite flow, with  $C = 20\%$ , moved out of the reservoir as a coherent mass without a clearly defined head (Fig. 8D). Minor folds developed in the slowly advancing mass of sediment, and tension cracks were present length-parallel to the flow direction in the two lowest folds (Fig. 8D).

**Flow velocities.**--- The head velocities of the bentonite flows and the kaolinite flows showed similar spatial patterns. This includes acceleration upon release from the reservoir to a maximum flow velocity that first increased and then decreased as a function of increasing suspended sediment concentration, followed by a phase of decelerating flow (Figs 6, 9). The maximum velocity of the bentonite flows increased from  $0.10 \text{ m s}^{-1}$  for  $C = 1\%$  to a peak of  $0.37 \text{ m s}^{-1}$  for  $C = 16\%$ , and then decreased to  $0.07 \text{ m s}^{-1}$  for  $C = 20\%$  (Figs 9, 11A). The rate of flow deceleration increased with increasing suspended sediment concentration for the flows that carried up to 10% bentonite. The 15% bentonite flow stopped before reaching the end of the flume, owing to a high rate of deceleration in the final flow phase. This phase of rapid deceleration is characteristic of all the bentonite flows with  $C \geq 15\%$ , but it occurred progressively closer to the lock gate, as the suspended sediment concentration was increased from 15% to 20% (Fig. 9B). All flows exhibited velocity fluctuations superimposed on the longer trend of decelerating flow. These fluctuations reached c.  $0.1 \text{ m s}^{-1}$  in the 15% flow, but remained below c.  $0.05 \text{ m s}^{-1}$  in the other bentonite flows.

**Deposits.**--- The flows with  $C \geq 15\%$  bentonite produced measurable run-out distances within the 4.69 m long tank. The deposits decreased in length from 4.66 m for  $C = 15\%$  to 0.22 m for  $C = 20\%$  (Figs 10, 11B). All the bentonite deposits were thickest near the back of the reservoir. The deposits of the 15-17% flows thinned steadily from within the reservoir to  $x \approx 1 \text{ m}$ . Thereafter, the bed thickness remained constant until the deposits terminated abruptly (Fig. 10). The 18% and 19% flows produced deposits with abrupt terminations as well, but these beds also contained a distinct, 0.03-0.04 m deep, depression at  $x \approx 0.60 \text{ m}$ . The flow laden with 20% bentonite produced a block-shaped deposit that was between 0.20 m and 0.29 m thick for most of its length, but at its termination the bed thickness reduced to zero over a distance of only 0.1 m.

#### *Comparison of flow velocities and run-out distances*

Figure 11 compares the maximum head velocities and run-out distances for the three sediment types as a function of initial suspended sediment concentration. Up to  $C = 10\%$ , the maximum head velocity,  $U_{h,m}$ , increased at a similar rate for these sediment types (Fig. 11A). As suspended sediment concentration was increased further, the  $U_{h,m}$ -values started to diverge, *e.g.*, attaining  $0.35 \text{ m s}^{-1}$  for bentonite,  $0.41 \text{ m s}^{-1}$  for kaolinite, and  $0.45 \text{ m s}^{-1}$  for silica flour at  $C = 15\%$ . The bentonite flows achieved the highest  $U_{h,m}$ -value at  $C = 16\%$ . With a further increase in bentonite concentration,  $U_{h,m}$  decreased rapidly until the bentonite was no longer able to flow out of the reservoir at an estimated  $C \approx 20.5\%$  (Fig. 11A). The  $C$ - $U_{h,m}$  curves for the bentonite, kaolinite and silica flour flows have a similar shape, but the maximum  $U_{h,m}$  and the suspended concentrations at which this maximum velocity was reached, were significant higher for kaolinite and silica flour. The kaolinite flows reached  $U_{h,m} = 0.50 \text{ m s}^{-1}$  at  $C = 22\%$ , and the silica flour flows attained  $U_{h,m} = 0.75 \text{ m s}^{-1}$  at  $C = 47\%$  (Fig. 11A). The kaolinite and silica flour suspensions failed to leave the reservoir at estimated  $C$ -values of 30.5% and 53%, respectively.

Within the confinement of the flume, the run-out distance of the sediment gravity flows strongly depended on concentration and clay type (Fig. 11B). Progressively less suspended sediment was required to produce a deposit of equal length for silica flour, kaolinite and bentonite. For example, the 19% bentonite flow had a run-out distance of 1.22 m, whereas 27% of kaolinite and 51% of silica flour were needed to achieve a similar run-out distance. 15% bentonite was required to produce deposits that were limited in length to the confinement of the flume (*i.e.*  $x = 4.69 \text{ m}$ ). This threshold concentration was much higher for kaolinite, at  $C = 22\%$ , and for silica flour, at  $C = 47\%$  (Fig. 11B).

## PROCESS INTERPRETATIONS

### *Silica flour flows*

Silica flour is composed of ground quartz and generally assumed non-cohesive (Parker et al. 1987; Baas et al. 2005; Felix and Peakall 2006; Kane et al. 2010). However, Pashley and Karaman (2005) found that silica flour particles may have a weak negative surface charge owing to the disassociation in water of some of the silanol ( $\text{SiOH}$ ) groups, thus rendering silica flour weakly cohesive. These weak to non-cohesive properties may have caused the silica flour flows in this study to behave differently from the stronger cohesive kaolinite and bentonite flows, particularly at high suspended sediment concentrations. However, other processes, such as frictional grain-to-grain interactions, dispersive pressure, and hindered settling, may have also controlled the behavior of the silica flour flows, as discussed below.

The flows laden with  $\leq 44\%$  silica flour behaved in a similar manner to many experimental turbidity currents described in the literature (Figs 2A, B; *e.g.*, Kuenen and Migliorini 1950; Middleton 1966;

Marr et al. 2001), in that they were visually fully turbulent, thus allowing the sediment particles to be supported by the upward velocity component of fluid turbulence (Middleton and Hampton 1973; Kneller and Buckee 2000). This behavior renders these silica flour flows low-density turbidity currents (LDTTC; Table 3), following the definition of Lowe (1982). These flows remained fast-moving and dynamic with pronounced Kelvin-Helmholtz instabilities at the upper boundary up to such high concentrations owing to the large density difference with the ambient water and the small size of the particles ( $D_{50} = 18.2 \mu\text{m}$ ). Consequently, turbulent energy within the flows was able to outcompete the particle settling velocity, and keep the particles in suspension. High dispersive pressure and hindered settling may also have helped the particles remain suspended in these flows (Middleton and Hampton 1973).

At  $C = 46\%$  to  $C = 50\%$ , the silica flour flows were classified as high-density turbidity currents (HDTTC; *sensu* Lowe, 1982; Table 3), as these flows comprised a dense lower zone 1 separated from a dilute upper zone 2 by a break in density (Fig. 2C). Zone 1 formed from the accumulation of particles near the base of the flow, and zone 2 resulted from shear-induced mixing of sediment within the upper part of the flow with the ambient water, thereby forming shear waves and Kelvin-Helmholtz instabilities that moved particles upward and ambient water downward. At  $C \geq 48\%$ , the mobility of the flows started to reduce progressively, resulting in full turbulence suppression and plug flow behavior in the 51% and 52% flows, which are classified herein as a non-cohesive mud flow (NCMF) and a slide, respectively, because the 51% suspension evolved into a flow with a flat upper boundary after sliding out of the reservoir, whereas the 52% suspension was arrested in the sliding phase (Table 3; Fig. 2D). At  $C \geq 48\%$ , the volumetric concentration of the flows was close to the cubic packing density of clastic sediment (c. 52%). It is therefore inferred that frictional grain-to-grain interactions prevented the development of turbulence within the flows at  $C \geq 48\%$ , thus outcompeting the effect of excess density, encouraging bulk settling, and slowing down the flows (Iverson 1997).

All the flows with  $C \geq 47\%$  showed a dilute suspension cloud that outran the main body of the flow (Fig. 2D). While the dense main body of the HDTTCs laden with 47% to 50% silica flour slowed and stopped, as the frictional forces outcompeted the excess density, the dilute suspension cloud was driven by turbulence and still had enough momentum to continue flowing. Minor erosion at the top of the 51% and 52% silica flour flows helped producing the dilute turbidity current, which was then able to travel slowly along the entire length of the tank.

In contrast to the kaolinite and bentonite flows herein and other high-density clay-laden SGFs described in the literature (Fig. 2; Marr et al. 2001; Elverhøi et al. 2005), none of the silica flour flows

hydroplaned. Hydroplaning occurs when the dynamic pressure generated in the ambient fluid just below the head of the flow approaches or exceeds the weight per unit area of the material in the head of the flow (Mohrig et al. 1998). Another requirement for hydroplaning is that the permeability of the base of the flow is low enough to prevent mixing of the overridden water into the flow above (Talling 2013). This may not have been achievable for the silica flour-laden flows due to the lack of cohesive strength in these flows. In the LDTCs and HDTCs in particular, the high turbulent energy and small particle size meant that any water forced underneath the head was rapidly mixed into the flow. The NCMF and slide may have had a permeable base as well, but these dense flows were probably also too heavy and did not travel quickly enough to allow water to be forced underneath the head of the flow.

The pointed semi-elliptical shape of the head of the silica flour flows with  $C \leq 48\%$  is commonly seen in turbidity currents of relatively low density and low cohesive strength, in which the head is shaped into a streamlined form, thus minimizing the pressure force at the front of the flow (Figs 2A-C; Hampton 1972; Middleton 1993). Although the 46% and 48% silica flour flows behaved as HDTCs, these flows apparently did not have enough internal strength to resist being shaped by the resistive shear forces and the no-slip condition on the upper and lower flow boundaries (Britter and Simpson 1978; Kneller and Buckee 2000). Conversely, the rounded shape of the head of the silica flour flows with  $C \geq 49\%$  suggests that these flows did have enough strength to resist being shaped by the hydrodynamic pressures. This strength may result from a variety of mechanisms: high dispersive pressure, hindered settling, frictional grain-to-grain interaction, and the weak negative surface charge of silica flour (Middleton and Hampton 1973; Iverson 1997; Pashley and Karaman 2005). The flows with  $C \geq 49\%$  also had relatively low head velocities, which reduced the hydrodynamic pressure on the head of these flows, and thus the ability to give the head a streamlined shape (Mohrig et al. 1998).

All the silica flour-laden flows accelerated to a maximum velocity upon leaving the reservoir (Fig. 3). The flows accelerated to a greater velocity with increasing volumetric concentration up to  $C = 47\%$ , as increasing the concentration increases the density difference between the sediment suspension and the ambient fluid, and it is this difference which drives the flow. However, for  $C \geq 48\%$ , further increasing the volume concentration reduced the maximum velocity that the flows accelerated to. It is suggested that friction from grain-to-grain interactions attenuated the turbulence within the flow and reduced the flow velocity at these high suspended sediment concentrations (Iverson 1997). As the concentration was increased, the frictional forces became greater and the mobility of the flows reduced, resulting in shorter run-out distances with increasing concentration for the flows carrying at least 47% silica flour (Figs 3B, 4).

The rate of deceleration of the head of the silica flour-laden flows increased as the suspended sediment concentration was increased. At  $C \leq 25\%$ , the flows decelerated relatively slowly, driven by resistive shear forces, along the length of the tank (Fig. 3A; Kneller and Buckee 2000). At higher concentrations, the flows displayed a faster rate of deceleration, especially at  $C \geq 47\%$ , where all the flows showed a rapid spatial decrease to zero velocity (Fig. 3B). Abrupt deceleration has been observed before for high-concentration silica flour flows produced in the laboratory (Hallworth and Huppert 1998). This rapid rate of deceleration is attributed to frictional freezing (Mutti et al. 1999; Mulder and Alexander 2001; Kane et al. 2009). As the flow starts to slow down, the vertical movement of the grains due to settling becomes greater than the horizontal movement, and the flow contracts vertically. This contraction process brings the particles in closer proximity, resulting in greater frictional forces, which further reduce the forward momentum of the particles. This negative feedback thus leads to rapid deceleration. The origin of the velocity fluctuations superimposed on the general trend of decelerating head velocity is unclear. These fluctuations may be attributed to the formation of elongate packets of sediment with contrasting velocity within lobes and clefts at the base of the flow, and interaction of the flow with waves on the water surface, produced by the displacement of ambient water upon release of the sediment suspension from the reservoir.

The HDTCs, NCMF, and slide with  $C \geq 47\%$  deposited all or most of the silica flour within c. 1 m of the lock gate, forming steeply inclined, wedge-shaped, sediment bodies (Fig. 4). This is further testament to the dominance of frictional forces over turbulent forces at these high suspended sediment concentrations. However, part of the sediment within the HDTCs was transported beyond  $x = 1$  m, suggesting that the remaining turbulent forces were able to keep part of the silica flour in suspension until frictional freezing commenced. The blocky shape of these deposits agrees well with the shape of deposits formed by natural high-density SGFs, such as in the Marnoso-arenacea Formation, Italy (Amy et al. 2005, their figure 3B).

The depression in the deposits of the 50% and 51% silica flour flows (Fig. 4) resembles those that Elverhøi et al. (2005) associated with flow 'stretching' due to hydroplaning, which causes the head of a dense flow to accelerate away from the body. However, the fact that the silica flour flows in the present study did not hydroplane suggests that other mechanisms may also create these depressions. It is hypothesized herein that differences in the forward velocity of the head, neck and body of the flow, related to local differences in suspended sediment concentration, are responsible for the flow stretching. If it is assumed that the head of the flow travels slower than the neck of the flow, because of resistive forces at the front of the flow, sediment particles are moved from the neck into the head. If then bulk settling of silica flour particles, as a result of turbulence suppression, and ensuing high yield stress in the body of the flow reduces the velocity so that the body cannot keep

up with the neck of the flow, the sediment pushed from the neck into the head is not replenished with sediment from the body of the flow. This would result in a depression in the deposit at the point where the body stops moving due to bulk settling and the neck and head of the flow keep some forward momentum. Velocity measurements within the 50% and 51% flows are needed to test this hypothesis. Finally, the 52% silica flour flow may not have produced a deposit with a depression, because of a lack of internal velocity gradients, which is typical for a slide moving as a rigid plug.

#### *Kaolinite and bentonite flows*

The kaolinite and bentonite flows with  $C \leq 15\%$  and  $C \leq 10\%$ , respectively, behaved as typical LDTCs (Table 3), fully dominated by turbulent mixing in the head and body of these flows (Middleton 1966; Middleton and Hampton 1973; Lowe, 1982; Sumner et al. 2009). The heads of these LDTCs maintained a pointed semi-elliptical shape, which minimized the pressure forces at the front of the flows.

At volume concentrations between 22% and 25% for kaolinite and between 15% and 17% for bentonite, the flows showed HDTC behavior (Table 3; Kuenen 1951; Lowe 1982). These clay-laden HDTCs can be classified as transient-turbulent, or transitional, flows (Wang and Plate 1996; Baas and Best 2002). Herein, the high concentration of clay particles in the lower part of the flows caused the transient-turbulent behavior. In this near-bed flow layer (zone 1), the probability for particles to collide, flocculate, and form gels, was high, which made the flows viscous, attain a higher cohesive strength, and thus become subjected to turbulence suppression (Baas et al. 2009).

This HDTC behavior was particularly prominent along most of the path of the 22% to 25% kaolinite flows and the 15% to 17% bentonite flows. All these flows comprised of a dense lower zone 1 that was distinct from a dilute upper zone 2, where mixing with ambient water through Kelvin-Helmholtz instabilities was observed (Figs 5A, B, 8A, B; Baas et al. 2004). The color difference between the two zones and the presence of interfacial waves was likely caused by a break in density. Although it cannot be ruled out that the formation of FES in zone 1 of the HDTCs was limited to the side wall of the flume, the presence of these FES implies that the flows had a high enough yield stress to limit turbulent mixing of the entrained water into the flow. Fluid escape took place during flow, which explains why the FES were often oriented at an angle to the vertical.

The 22% kaolinite flow and the 17% bentonite flow produced a tripartite structure along part of their flow path (Figs 5A, 8B). The basal zone 1a in the 22% kaolinite flow was featureless, while this zone contained horizontal sheets of water in the 17% bentonite flow (Fig. 8B), which appeared to form by injection of water at the flow front. The formation of FES in zone 1b of both flows suggests that this

zone had a slightly lower cohesive strength than zone 1a. The flows were probably too slow, and therefore too cohesive, to develop the tripartite structure in the early and late flow stages. Instead, the two-partite structure, discussed above, prevailed. Alternatively, the two-partite flow structures may have remained after deposition of clay from basal zone 1a in the final flow stages.

The 15% and 16% bentonite flows carried packets of cohesive sediment, which formed when small sections of cohesive sediment were torn off zone 1 by ambient water forced over the front of the flows (Fig. 8A). This suggests that the shear force imposed by this ambient water exceeded the yield stress of the sediment suspension. These packets of bentonite were cohesive enough to resist mixing with the ambient water, as they were thrown over the top of the head. Yet, these packets were seen to disintegrate and become incorporated within the dilute mixing zone 2 under the influence of high turbulence. Packets that were carried along at the base of the head survived for longer, presumably because the shear forces at the base of zone 1 were weaker than near the top of zone 2.

The concentration of clay particles within the flows that carried more than 25% kaolinite or more than 17% bentonite appeared high enough to form clay gels, *i.e.*, pervasive, volume-filling networks of clay particle bonds, throughout the flow (Figs 5C, D, 8C, D; Baas et al. 2009). These gels are inferred to have had a high enough yield stress to form rigid plug flows without internal turbulence, typical of debris flows (Middleton and Hampton 1973; Baas et al. 2009). The kaolinite flows with  $C = 27\%$  and the bentonite flows with  $C = 18\%$  and  $C = 19\%$  are classified herein as cohesive mud flows (CMF; Table 3). The high yield stress of these CMFs is further supported by the sharply reduced mixing with the ambient water, although the relatively weak water flow across the upper flow boundary at these high  $C$ -values may also have prevented the bonds between the clay particles from breaking on a large scale. Likewise, mixing at the top of the 29% kaolinite flow and 20% bentonite flow was negligible as a consequence of the particularly high cohesive strength and low head velocity. These flows were classified as slides, following the definition of a high-density SGF that moves as a coherent mass without significant internal deformation (Figs 5D, 8D; Table 3; Martinsen 1994; Mohrig and Marr, 2003), and the fact that these flows were arrested in the sliding phase soon after the gate had been lifted, similar to the 52% silica flour flow.

The presence of tension cracks on top of the 27% kaolinite flow and the 19% bentonite flow suggests that these flows were cohesive enough to have tensile strength and that these flows were placed under flow-parallel tension (Fig. 5C; Marr et al. 2001). Small spatio-temporal variations in flow velocity, partly related to hydroplaning, may have put these flows under tension. The 20% bentonite slide also exhibited tension cracks, but these were oriented parallel to the direction of movement of

the slide. These cracks formed, because the flow moved at a slightly faster rate in the center of the flume than at the sidewall, thus placing it under tension perpendicular to the movement direction.

The shape of the head of the clay flows with high  $C$ -values can be related to their rheological properties as well as the hydrodynamic pressure at the front of these flows (Mohrig et al. 1998). Unlike the flows with  $C \leq 22\%$  kaolinite and  $C \leq 17\%$  bentonite, which all had semi-elliptically shaped heads, the head of the 25% kaolinite flow attained a rounded shape for part of its flow path (Fig. 5B). It is inferred that, owing to the high cohesive strength of this flow, the hydrodynamic pressures were not able to change the head of this flow into a more streamlined shape. The particularly thin pointed semi-elliptically shaped head of the 27% kaolinite flow and the blunt, semi-circularly shaped head of the 29% kaolinite flow also support the interpretation that these high-density flows were cohesive enough to withstand streamlining by ambient water swept over the front and top of these flows (Figs 5C, D). The roller waves in the heads of the 18% and 19% bentonite flows were particularly striking (Fig. 8C). Hampton (1972) also observed “blunt snouts with a sharp-tipped crest curled back over the top of the flow” in debris flows with a low water content (below 70% by weight). Hampton (1972) attributed this shape to the high yield stress of the flows, which allowed the water pushed back over the top of the head to create a fold that was able to resist erosion and maintain the sharp-tipped crest.

The kaolinite flows with  $22\% \leq C \leq 27\%$  and the bentonite flows with  $15\% \leq C \leq 19\%$  hydroplaned along parts of their flow path (Figs 5A, B, 8A-C). This implies that the dynamic pressure generated in the ambient fluid below the front of these flows approached or exceeded the weight per unit area of the sediment in the head of the flows (Mohrig et al. 1998), and that the permeability at the base of these flows was low enough to prevent mixing of the overridden water into the flow above (Talling 2013). Here, it is assumed that the latter criterion was not met in the flows with lower clay concentration, because the high level of turbulence quickly mixed the overridden water into the base of the flows. In the 29% kaolinite and 20% bentonite flows, the weight per unit area of the sediment in the head is inferred to have been too large to allow hydroplaning to develop (Figs 5D, 8D). Hydroplaning did not take place either in the initial and final stages of the kaolinite flows with  $22\% \leq C \leq 27\%$  and the bentonite flows with  $15\% \leq C \leq 19\%$ . Near the reservoir, the hydrodynamic pressures at the front of the head needed time to support the downward directed weight of the flow and force a thin layer of water underneath the head (Mohrig et al. 1998; Talling 2013). As the flows slowed during their final stages, the hydrodynamic pressure at the front of the head reduced and might not have been able to support the weight of the flows any longer, thus causing hydroplaning to terminate (Mohrig et al. 1998).

The balance between turbulent and cohesive forces can also be used to explain the observed trends in head velocity and run-out distance of the clay flows (Figs 6, 9). For the fully turbulent  $C \leq 15\%$  kaolinite and  $C \leq 10\%$  bentonite LDTs, the progressive increase in head velocity with increasing volumetric concentration resulted from the density difference driving the flows (Figs 6A, 9A). We interpret that at these concentrations the cohesive forces did not influence the flow dynamics. This is further confirmed by the relatively slow deceleration of these flows along the length of the tank, which is inferred to result from effective particle support by shear turbulence and minor particle settling (Figs 6A, 9A).

In the flows that carried more than 22% kaolinite and more than 16% bentonite, the maximum head velocity started to decrease, as  $C$  was increased, because the cohesive forces became stronger than the turbulent forces within these flows, despite the large density difference with the ambient water. This lack of turbulent support, combined with bulk settling of the clay gel, resulted in stronger spatial deceleration of the flow and shorter run-out distances of the deposits of these flows (Figs 7, 10). These flows decelerated particularly quickly in the final stage, which is considered to result from 'cohesive freezing' (Mulder and Alexander 2001). As the flow starts to slow down, lower turbulent forces and flow contraction due to bulk settling allow the clay particles to form a greater number of electrostatic bonds and increase the cohesive strength of the flows. In turn, this further reduces the turbulence and encourages even greater cohesive strength. This negative feedback mechanism allows clay flows to decelerate very quickly. Jacobson and Testik (2013) also produced laboratory flows composed of kaolinite with abrupt transitions, which they attributed to the presence of a lutocline, which, combined with the non-Newtonian rheology of the clay, suppressed the turbulence. As with the silica flour flows, the high-frequency head velocity fluctuations in the clay flows could have been related to the formation of lobes and clefts, and waves on the water surface.

The length of the flume limited the acquisition of a full range of runout distances for the LDTs and HDTs. Within the available range of data, suspended sediment concentration shows an inverse, linear, relationship with runout distance (Fig. 11B). Similar to the deposits of the silica flour flows, the deposits of the clay flows changed from wedge-shaped with a block-shaped extension to wedge-shaped without an extension, as the flow type changed from HDTC via CMF to slide (Figs 7, 10; Table 3). The deposits of the 25% and 27% kaolinite flows and the 18% and 19% bentonite flows showed distinct depressions (Figs 7, 10; Table 3), analogous to the depressions described for the deposits of the 50% and 51% silica flour flows. This range of shapes can therefore be interpreted in a similar way, yet with cohesive force rather than frictional force competing against turbulent forces for the clay-laden flows. Hence, strong cohesive forces caused rapid bulk settling of clay gels within the reservoir and down to  $x = 1$  m, and turbulent forces within the HDTs were able to move part of the

clay into the flume and form block-shaped deposits with an abrupt termination associated with cohesive freezing. The flow stretching mechanism of Elverhøi et al. (2005) explains the depression in the deposits of the flows that showed hydroplaning. Interestingly, hydroplaning below the 25% kaolinite flows appeared to have encouraged the head to detach completely from the body and form an outrunner block. This zero-thickness depression was found 1.37 m behind the front of the deposit, implying that the detached head stretched after separating from the body. Variations in the forward velocity of the head, neck and body of the flows, which was used to explain the origin of the depression in the deposits of the high-concentration silica flour flows, may also apply to the clay flows. A lack of hydroplaning and internal variations in flow velocity explain the absence of a depression in the slides laden with kaolinite and bentonite, which had such a strong network of clay particle bonds that they only flowed a short distance from the reservoir.

## **TOWARDS A UNIFIED MODEL FOR HEAD VELOCITY AND RUN-OUT DISTANCE**

### *Effect of sediment type on maximum head velocity and run-out distance*

A comparison of the flows and the deposits for the three sediment types reveals large differences, mostly relating to their contrasting rheological properties. From silica flour via kaolinite to bentonite, a progressively smaller volumetric suspended sediment concentration is required to produce a comparable runout distance (Fig. 11B). This suggests that the density difference between flow and ambient water as well as the type of sediment controlled the runout distance. Bentonite clay is more cohesive than kaolinite clay (Yong et al. 2012). Bentonite therefore creates a stronger network of particle bonds and resists stronger turbulent forces than kaolinite at similar suspended sediment concentrations, leading to weaker particle support and shorter runout distances. Extremely high concentrations of silica flour were needed to produce flows with a comparable runout distance to the kaolinite and bentonite flows. The fully or near to cohesionless nature of silica flour impedes electrostatic forces that encourage particle attractions (Baas et al. 2005; Felix and Peakall 2006). Therefore, very high suspended sediment concentrations are needed to make the flow sufficiently viscous and produce enough frictional strength between individual particles to suppress turbulence and thus resist the density difference between the suspension and the ambient water, which drives the flow at lower  $C$ -values (Mutti et al. 1999; Kane et al. 2009).

For flows with  $C \leq 10\%$ , the maximum head velocity increased with increasing sediment concentration in a similar way across the three sediment types (Fig. 11A). This implies that the flows were driven purely by the density difference at these low concentrations, and that any cohesive and frictional forces were unable to attenuate the turbulence. For flows with  $C > 10\%$ , the maximum head velocities started to diverge, and the cohesive forces within the kaolinite and bentonite flows

started to influence the dynamic structure of these flows by attenuating the turbulence, changing the flows from turbulent to transitional (Baas et al. 2009). However, the density difference remained the dominant driving force, considering the positive correlation between maximum head velocity and suspended sediment concentration (Fig. 11A). The maximum head velocity of the clay flows kept increasing at a decreasing rate until a maximum was reached, which is inferred to indicate the stage where flow deceleration by gelling exceeds flow acceleration by density difference. The experimental data also show that a stronger balance in favor of cohesive and frictional forces produces a rapid reduction in the maximum head velocity of the flows with increasing volume concentration, once the maximum  $U_{h,m}$ -value has been exceeded (Fig. 11A). The maximum head velocity of the bentonite flows was consistently lower than that of the kaolinite flows for  $C \geq 15\%$ , showing the ability of the bentonite to form a stronger network of particle bonds than the kaolinite. Remarkably, the non-cohesive silica flour flows remained fully turbulent for all  $C$ -values where the kaolinite and bentonite flows behaved as HDTCs, CMFs, and slides, or were too cohesive to flow at all. The silica flour also produced a convex upward curve in Fig. 11A, but for this sediment type frictional forces, rather than cohesive forces, started to outcompete the excess density at much higher concentrations than for kaolinite and bentonite.

#### *Dimensional analysis of maximum head velocity and run-out distance*

Figure 11A reveals that the bentonite, kaolinite, and silica flour flows reacted in a similar way to changes in initial suspended sediment concentration, driven by density difference at low  $C$ -values and by cohesive and frictional forces at high  $C$ -values. It should therefore be possible to describe the changes in flow behavior in terms of differences in rheological properties. Below, it is shown that the initial yield stress of the clay suspension in the reservoir can be used to delineate flow type, determine a dimensionless maximum head velocity and determine a run-out distance largely independent of clay type. We hypothesized that the yield stress governs the ability of the clay suspension to leave the reservoir after lifting the lock gate. If the suspension is able to move out of the reservoir, this yield stress then controls the spatial evolution of the head velocity and the run-out distance of the flow related to the conversion from potential energy to kinetic energy. Testing this hypothesis required several analytical steps: (a) non-dimensionalising the velocity curves in Fig. 11A, so that the data collapse onto a single curve; (b) determining functional relationships between sediment concentration and initial yield stress, based on the available rheometrical data for bentonite and kaolinite; (c) converting the collapsed curve for head velocity from dimensionless sediment concentration to yield stress; (d) delimiting initial yield stress ranges for LDTCs, HDTCs, mud flows and slides, and; (e) establishing a functional relationship between initial yield stress and run-out distance.

The maximum head velocities for the experimental bentonite, kaolinite, and silica flour flows (Fig. 11A) were collapsed using the following best-fit equations:

$$\frac{U_h}{U_{h,m}} = \left( \frac{C}{C_m} \right)^{0.466}, \quad \text{for } 0 < C \leq C_m, \quad (1a)$$

$$\frac{U_h}{U_{h,m}} = 1 - \left( \frac{C - C_m}{C_0 - C_m} \right)^{2.82}, \quad \text{for } C_m < C \leq C_m, \quad (1b)$$

where  $U_h$  is the maximum head velocity of the flow,  $U_{h,m}$  is the highest value of  $U_h$  for the sediment type under consideration (*i.e.*,  $0.75 \text{ m s}^{-1}$  for silica flour,  $0.50 \text{ m s}^{-1}$  for kaolinite, and  $0.37 \text{ m s}^{-1}$  for bentonite; Table 2),  $C_m$  is the suspended sediment concentration at  $U_{h,m}$  (47% for silica flour, 22% for kaolinite, and 16% for bentonite), and  $C_0$  is the threshold concentration above which the flow is not mobile enough to leave the reservoir ( $U_h = 0$ ). The  $C_0$ -values were derived by extrapolation of the experimental data to  $U_h = 0$ , yielding 20.5% for bentonite, 30.5% for kaolinite, and 53% for silica flour.

The best-fit Equations 1a and 1b have high  $R^2$  values (Fig. 12), confirming that the head velocity curves for the bentonite, kaolinite, and silica flour flows have a similar profile. Equation 1a describes the effect of density difference on head velocity in flows where turbulence is dominant, and cohesive and frictional forces have a small influence on flow dynamics, or no influence at all. The power in Equation 1a is similar to the power of 0.5 in the well-known relationship between density difference and head velocity for experimental density currents of Middleton (1966):

$$U_h = 0.75 \left[ \frac{(\rho_f - \rho_a)gH}{\rho_a} \right]^{0.5}, \quad (2)$$

where  $\rho_f$  is the flow density,  $\rho_a$  is the density of the ambient water,  $g$  is the gravity constant, and  $H$  is the flow thickness. Here,  $\rho_f = \rho_s C + \rho_a(1 - C) = \rho_a[C(s - 1) + 1]$ , where  $\rho_s$  is the sediment density, and  $s$  is the specific density of the sediment,  $\rho_s/\rho_a$ . The square-bracketed term in Equation 2 is equal to  $(g'H)^{1/2}$ , where  $g'H = g_s'C$  is the reduced gravity of the sediment, where  $g_s' = (1 - s)g$ . Since the densimetric Froude number is defined by  $Fr' = U_h/(g'H)^{1/2}$ , Equation 2 states that the head velocity is governed by a densimetric Froude number of 0.75. Each head velocity in Table 2 has a Froude number associated with it, which was determined using the position,  $x_{h_v}$ , of the maximum head velocity in the profiles in Figs 3, 6 and 9, and the conservation of volume per unit width re-arranged for flow thickness  $H = A/(0.31 + x_{h_v})$ , where  $A = 0.1085 \text{ m}^2$  is the cross-sectional area of the reservoir, and 0.31 m refers to the length of the reservoir. Table 2 shows that  $Fr' = 0.75$  is reasonable for most experiments. However, there were experiments where  $Fr' > 1$ , which correspond to  $U_h$ -values occurring at greater distances from the reservoir gate (*e.g.*, Figs 6 and 9). This procedure is consistent with Huppert and Simpson's (1980) Froude number parameterization of gravity flow in

terms of the flow height to water depth ratio. Equation 1b describes the flows where the cohesive and frictional forces outbalanced the density difference and reduced the head velocity. The effect of these forces on head velocity is exponential, probably because the clay gelling and frictional interaction also caused rapid loss of turbulent particle support. Below, the exponents in Equations 1a and 1b are rounded to 0.5 and 3, respectively. These approximations do not cause a significant reduction in the  $R^2$ -values.

In the next step of the dimensional analysis, the dimensionless maximum head velocity,  $U_h/U_{h,m}$ , was related to the initial yield stress,  $\tau_y$ , by using the dependence of yield stress on suspended clay concentration, summarized in Table 2. These rheometrical data are available only for kaolinite and bentonite clay at volume concentrations greater than 1% (Table 2). The yield stresses for the bentonite and kaolinite suspensions that produced the flows with maximum head velocities driven by the density difference with the ambient water ( $C \leq C_m$ ) collapse well if plotted against  $C/C_m$  (Fig. 13A). This relationship can be described by a power law:

$$\tau_y = \tau_{y,m} (C/C_m)^3, \text{ for } 0 < C \leq C_m, \quad (3a)$$

with  $R^2 = 0.94$  and  $\tau_{y,m} = 37.9 \text{ N m}^{-2}$ .  $\tau_{y,m}$  is the yield stress at  $U_h = U_{h,m}$  and  $C = C_m$ . Hence,  $37.9 \text{ N m}^{-2}$  is the estimated initial yield stress at which the flow maximum head velocity changed from being dominated by the density difference with the ambient water to being dominated by cohesive forces, independent of clay type. The yield stresses of the bentonite and kaolinite suspensions that produced the flows with maximum head velocities dominated by cohesion ( $C > C_m$ ) collapse if plotted against  $(C-C_m)/(C_0-C_m)$  (Fig. 13B):

$$\tau_y = \tau_{y,m} + (\tau_{y,0} - \tau_{y,m}) \left( \frac{C-C_m}{C_0-C_m} \right)^3, \text{ for } C_m < C \leq C_0, \quad (3b)$$

where  $\tau_{y,0} = 271 \text{ N m}^{-2}$ .  $\tau_{y,0}$  is the estimated yield stress at  $C = C_0$  and  $U_h = 0$ , thus representing the yield stress above which the clay suspensions did not leave the reservoir, regardless of clay type.

Equations 1a, 1b, 3a and 3b can now be combined to derive relationships between  $\tau_y$  and  $U_h/U_{h,m}$  (Fig. 14):

$$\frac{U_h}{U_{h,m}} = \left( \frac{\tau_y}{\tau_{y,m}} \right)^{1/6}, \text{ for } 0 < \tau_y \leq \tau_{y,m}, \quad (4a)$$

$$\frac{U_h}{U_{h,m}} = \frac{\tau_{y,0} - \tau_y}{\tau_{y,0} - \tau_{y,m}}, \text{ for } \tau_{y,m} < \tau_y \leq \tau_{y,0} \quad (4b)$$

In experiments where the runout distance was beyond the end of the tank, Hallworth et al.'s (1998) box model was used to estimate the expected run-out distance. This model, which is for non-

cohesive flows, assumes that the Froude number at the head of the flow is constant, the volume is conserved, and the settling is unhindered. The run-out distance,  $x_0$ , corresponding to the time for all the sediment to settle out, is:

$$x_0 = 1.6 [0.351 g_s' C A^3 / w_s^2]^{1/5} \quad (5)$$

where  $w_s = g_s' D_{50}^2 / 18\nu$  is the Stokes settling velocity, and  $\nu$  is the kinematic viscosity. Hallworth and Huppert (1998) demonstrated that Hallworth et al.'s (1998) model predicts the run-out distance well, provided that  $C < 15\%$ . It can be shown that the  $x_0$ -values calculated from Equation 5 for  $1\% \leq C \leq 15\%$  in the present experiments are greater than 4.69 m (cf. Fig. 15A).

The dependence of run-out distance on concentration for the high-concentration flows in Fig. 11B is approximately linear. Therefore, anticipating that there is a crossover between this straight line fit and the run-out distance of the low-concentration flows, predicted by Equation 5, a composite best-fit equation for  $x_0/x_{0,m}$  can be defined as:

$$\frac{x_0}{x_{0,m}} = \left( \frac{C}{C_{m1}} \right)^{1/5}, \quad \text{for } 0 < C \leq C_{m1}, \quad (6a)$$

$$\frac{x_0}{x_{0,m}} = \frac{C_0 - C}{C_0 - C_{m1}}, \quad \text{for } C_{m1} < C \leq C_0, \quad (6b)$$

where  $C_{m1}$  is the concentration at which the maximum run-out distance,  $x_{0,m}$ , is reached,  $C_{m1} < C_m$ , and  $x_{0,m} = 1.6[0.351 g_s' C_{m1} A^3 / w_s^2]^{1/5}$ , with  $C_{m1} = 14.8\%$  for silica flour,  $C_{m1} = 0.034\%$  for kaolinite and  $C_{m1} = 0.01\%$  for bentonite. Interestingly, the maximum run-out distances are similar for all three sediments:  $x_{0,m} = 27.1$  m for silica flour,  $x_{0,m} = 14.1$  m for kaolinite, and  $x_{0,m} = 16.9$  m for bentonite (Fig. 15A). The linear fit to the data based on Equation 6b yielded  $R^2 = 0.97$  (Fig. 15B).

Equations 3 and 6 can now be combined to derive relationships between  $\tau_y$  and  $x_0/x_{0,m}$ :

$$\frac{x_0}{x_{0,m}} = \begin{cases} \left( \frac{\tau_y}{\tau_{y,m1}} \right)^{1/15}, & \text{for } 0 < \tau_y \leq \tau_{y,m1}, \\ \frac{C_0 - C_m(\tau_y/\tau_{y,m})^{1/3}}{C_0 - C_{m1}}, & \text{for } \tau_{y,m1} < \tau_y \leq \tau_{y,m}, \\ \left( \frac{C_0 - C_m}{C_0 - C_{m1}} \right) \left[ 1 - \left( \frac{\tau_y - \tau_{y,m}}{\tau_{y,0} - \tau_{y,m}} \right)^{1/3} \right], & \text{for } \tau_{y,m} < \tau_y \leq \tau_{y,0}, \end{cases} \quad (7)$$

where  $\tau_{y,m1} = \tau_{y,m}(C_{m1}/C_m)^3$ , with  $\tau_{y,m1} = 1.3 \times 10^{-7}$  N m<sup>-2</sup> for kaolinite and  $\tau_{y,m1} = 8.4 \times 10^{-9}$  N m<sup>-2</sup> for bentonite. Since  $C_{m1}$  and  $\tau_{y,m1}$  for kaolinite and bentonite are small compared to  $C_0$  and  $\tau_y$ , Equation 7 can be approximated by:

$$\frac{x_0}{x_{0,m}} = \left( 1 - \frac{C_m}{C_0} \right) \left( \frac{\tau_y}{\tau_{y,m}} \right)^{1/3}, \quad \text{for } 0 < \tau_y \leq \tau_{y,m}, \quad (8a)$$

$$\frac{x_0}{x_{0,m}} = \left( 1 - \frac{C_m}{C_0} \right) \left[ 1 - \left( \frac{\tau_y - \tau_{y,m}}{\tau_{y,0} - \tau_{y,m}} \right)^{1/3} \right], \quad \text{for } \tau_{y,m} < \tau_y \leq \tau_{y,0}, \quad (8b)$$

with  $x_0$  ultimately tending to zero as  $\tau_{y,0}$  tends to zero. In Equation 8, only  $x_{0,m}$  is dependent on the box model. Figure 16 shows the relationship between  $x_0/x_{0,m}$  and yield stress for kaolinite and bentonite. Most of the variation in  $x_0/x_{0,m}$  is controlled by  $\tau_y$ . However, there is also some variation caused by sediment type as a result of  $C_m/C_0$  in Equation 8, with  $C_m/C_0 = 0.72$  for kaolinite and  $C_m/C_0 = 0.78$  for bentonite. Averaging this small variation, and taking an average  $x_{0,m}$ -value of 15.5 m from Fig. 15A, yield the following relationships between  $x_0$  and  $\tau_y$ :

$$x_0 = 0.25x_{0,m} \left( \frac{\tau_y}{\tau_{y,m}} \right)^{1/3}, \quad \text{for } 0 < \tau_y \leq \tau_{y,m}, \quad (9a)$$

$$x_0 = 0.25x_{0,m} \left[ 1 - \left( \frac{\tau_y - \tau_{y,m}}{\tau_{y,0} - \tau_{y,m}} \right)^{1/3} \right], \quad \text{for } \tau_{y,m} < \tau_y \leq \tau_{y,0}, \quad (9b)$$

As  $\tau_{y,m}$  and  $\tau_{y,0}$  are also constant, Equation 9 thus supports the hypothesis that the yield stress of the clay suspensions in the reservoir governs the travel distance of the clay flows after lifting the lock gate.

## YIELD STRESS AS AN INDEPENDENT PARAMETER TO DESCRIBE FLOWS AND DEPOSITS

The above dimensional analysis demonstrates that fine-grained SGFs go through similar stages of flow dynamics and deposit properties with increasing initial suspended sediment concentration. The differences in the cohesive properties of the clay suspensions were accounted for by converting suspended sediment concentration to yield stress. This indicates that yield stress is a primary control on the head velocity and the run-out distance. Equation 4 allows  $U_h/U_{h,m}$  of a cohesive SGF to be estimated from the initial yield stress in a straightforward manner, independent of clay type. In addition, Equation 9 provides a simple tool for computing the runout distance of a cohesive SGF from its initial yield stress, also independent of clay type. At present, however, the determination of the maximum head velocity requires knowledge of  $U_{h,m}$ , which is dependent on clay type. The dimensional analysis is based on the initial  $\tau_y$ -value of the suspensions within the reservoir. Once flowing out of the reservoir, the yield stress of these suspensions can be expected to vary in space and time as a result of mixing with ambient water and sediment deposition, as clay bonds break and reform under the changing flow stresses. However, the results of the dimensional analysis imply that these variations have little effect on the non-dimensional maximum head velocity and the run-out distance of these experimental flows, if the yield stress of the bentonite and kaolinite clay in the reservoir is identical.

Table 3 summarizes the properties of the LDTCs, HDTCs, mud flows and slides, and their deposits. Despite the large differences in initial suspended sediment concentration of the three types of sediment, these flow types have similar shapes, internal dynamics, and deposit shapes. The HDTCs produced deposits that were wedge-shaped with a block-shaped extension, the CMFs and NCMF produced wedge-shaped deposits with outrunner blocks, and the slides produced wedge-shaped deposits without extension (Table 3). These deposit shapes were clearly linked to the flow behavior of the fine-grained SGFs and the balance between the processes that promote and impede flow. The properties of the four flow types and their deposits are bracketed in terms of yield stress in Table 3. LDTCs change to HDTCs at  $\tau_y$ -values of c. 16-22 N m<sup>-2</sup>, the boundary between HDTCs and CMFs is at  $\tau_y \approx 67$ -94 N m<sup>-2</sup>, and slides are stable between  $\tau_y \approx 119$ -141 N m<sup>-2</sup> and  $\tau_y \approx 271$  N m<sup>-2</sup>.

## WIDER IMPLICATIONS

The present laboratory experiments are a suitable starting point for determining the dynamic properties, run-out distance, and deposit geometry of fine-grained SGFs in the natural environment, based on differences in rheology. However, quantitative scaling of the experimental results to natural flows and their deposits is not possible at present, principally because the best-fit coefficients in Equations 1 and 4-9 and the value of  $\tau_{y,m}$  might be dependent on the experimental setup. For example, the experiments were limited to flows carrying a single sediment type and moving across a horizontal bed with a low bed roughness, and to a single set of potential energies, controlled by the height of the suspension column in the reservoir.

Notwithstanding these limitations, the experimental data can be used to make a qualitative comparison with full-scale flows in nature. The laboratory flows with  $C \leq 10\%$  behaved in a similar manner for the three sediment types, with turbulence dominating these flows and the sediment particles unable to form high enough frictional forces or electrostatic forces of attraction to limit flow mobility. It is expected that the shape of the deposits of these low-density turbidity currents is also independent of the cohesive properties of the sediment, although a longer lock-exchange tank is needed to test this hypothesis. Based on previous work (*e.g.*, Middleton 1967; Lüthi 1981; Bonnecaze et al. 1993; Amy et al. 2005), these turbidite deposits should be elongate, thin and wedge-shaped. The threshold concentration of 10% might be higher for natural flows, since full-scale turbidity currents are often more turbulent (Talling et al. 2013), and therefore more likely to break the bonds between clay particles, than laboratory-scale turbidity currents. For practical purposes, this outcome implies that the deposits of clay-sized and fine-silt sized LDTCs can be interpreted in terms of turbulence properties and density difference with the ambient water, and that the type of sediment and yield stress can be ignored, even if these flows carry strongly cohesive clay minerals,

such as bentonite. In other words, clay- and silt-laden LDTCs have similar flow efficiencies (*sensu* Mutti et al. 1999)

In contrast, the type of sediment and the yield stress need to be taken into account for most HDTCs, mud flows, and slides. These high-density SGFs should generally transport weakly cohesive kaolinite over a greater distance than strongly cohesive bentonite, whilst non-cohesive fine-grained SGFs are inferred to travel the greatest distance from the origin. Hence, the flow efficiency of HDTCs, mud flows, and slides is generally lower for bentonite than for kaolinite (Mutti et al. 1999). The high efficiency of the laboratory flows laden with up to 47% silica flour is remarkable, and the anticipated implications for natural flows are significant. These laboratory flows were driven by a high density difference with the ambient water, high turbulence intensity, and low particle settling velocity. Natural turbidity currents may be at least one order of magnitude faster than in the laboratory (Talling et al. 2013). Since turbulence intensity increases with increasing flow velocity (*e.g.*, Baas et al. 2009), natural turbidity currents should be able to carry large volumes of silt-sized particles over long distances. This high sediment flux and long transport distance may even extend to sand-sized particles (*cf.*, Talling et al. 2007), if turbulent forces are sufficiently strong to keep the sand particles in suspension and frictional forces between the sand particles are weak. It is clear that the run-out distance of SGFs also depends on other factors, such as flow volume, basin floor morphology and the ratio of cohesive to non-cohesive sediment (Talling 2013). However, it is concluded here that fine sediment type is a major control above suspended sediment concentrations that are equivalent to the laboratory threshold of 10%, and that flow efficiency reaches a maximum value at which frictional and cohesive forces become dominant over density difference and particle support by turbulence. Once past this maximum, the flow efficiency rapidly decreases.

The rheological control on flow properties may also have significant implications for the geometry of high-density SGF deposits. It is expected that, at similar *C*-values, the deposits of high-density SGFs laden with weakly cohesive clay cover a larger surface area and have a smaller bed thickness than the deposits of high-density SGFs laden with strongly cohesive clay. Conversely, weakly cohesive clay beds may be thicker than their strongly cohesive equivalents, if these beds were formed by flows with the same initial yield strength, because flows laden with strongly cohesive clay carry a smaller volume of sediment, and were predicted to have approximately the same run-out distance as the flows laden with weakly cohesive clay (Fig. 16; Equation 9).

Kaolinite and bentonite are the weakly and strongly cohesive end members of a suite of clay minerals that are common in nature (Table 1). Illite and chlorite are clay minerals of intermediate cohesive strength. Further work is needed to verify if the rheological model for kaolinite and

bentonite SGFs presented in this study is also valid for chlorite and illite SGFs, and also stretches to SGFs that carry mixtures of clay minerals. This study covered the entire spectrum from non-cohesive to strongly cohesive sediment, so it is appropriate to hypothesize that measuring the relationship between yield stress and suspended sediment concentration for, for example, illite, chlorite and mixed clay minerals. is sufficient to determine the flow dynamics, run-out distance and deposit shape of SGFs laden with these types of sediments, notwithstanding the limitations described above. This hypothesis assumes that other clay minerals do not have more complex rheological properties than kaolinite and bentonite.

With time, recurring SGF events build the architecture of larger-scale sediment bodies, such as channel fills, levees, and lobes in submarine fans. It follows from the above discussion that this architecture may be different for flows that carry different types of clay minerals and non-cohesive fine sediment, especially if HDTCs, mud flows and slides constitute a major portion of this architecture. Other potential geological applications of this study include: (i) a better delineation of the rheological properties of SGFs that form LDTC deposits, HDTC deposits, debris flows, slides in core and outcrop, and; (ii) rheological characterization of modern turbidity currents in lakes and oceans, based on novel techniques for measuring flow velocity and suspended sediment concentration (*e.g.*, Sumner and Paull 2014).

## CONCLUSIONS

The present laboratory experiments show that both sediment type and suspended sediment concentration control the flow properties and the deposits of fine-grained SGFs. At low concentrations, the dominant turbulent forces prevent electrochemical binding and frictional interaction between the particles, and the density difference with the ambient water drives the flow, thus producing similar behavior between flows laden with sediment of contrasting cohesive properties. At high concentrations, however, cohesive and frictional forces outbalance turbulent forces, leading to decreased particle support within the flow. Consequently, non-cohesive silica flour flows produce a greater run-out distance and a higher maximum head velocity than weakly cohesive kaolinite flows of similar density. This difference in flow behavior is even greater for strongly cohesive bentonite flows, which have the shortest run-out distances and the lowest maximum head velocities. The change in flow behavior controlled by density difference and turbulent forces to flow behavior controlled by cohesive or frictional forces increased from 16% for bentonite via 22% for kaolinite to 47% for silica flour. This threshold concentration for the silica flour flows is close to the cubic packing density of clastic sediment, which supports the idea that non-cohesive fine-grained

SGFs are turbulent and highly mobile up to very high densities, and friction between particles in an extremely dense suspension is required to impede flow.

The SGFs laden with silica flour, kaolinite, and bentonite all changed from LDTs via HDTs and mud flows to slides, as the suspended sediment concentration was increased. Within the limits of the experimental setup, these flow types have similar flow properties and produce similar deposit shapes. The initial yield stress of the pre-failure suspension defines the transition between these flow types, and the initial yield stress also governs the dimensionless maximum head velocity and the run-out distance of these SGFs, independent of clay type. In other words, the present study demonstrates that yield stress is a primary control on the momentum and the run-out distance of fine-grained sediment gravity flows.

This laboratory study provides an exciting platform for increasing the understanding and the predictive ability of the shape and the run-out length of the deposits of natural fine-grained SGFs. The effect of the cohesive properties of the suspended sediment on deposit geometry can be ignored only at  $C \leq 10\%$ . Above this concentration, the run-out length of the deposits increases, as the cohesive properties of the suspended sediment decrease. However, it should be noted that this threshold concentration is probably higher for natural flows, because these are often more turbulent than the laboratory flows. The differences in the geometry of deposits from flows laden with fine-grained sediment of contrasting cohesive strength may be reflected in differences in the architecture of stacked fine-grained SGF deposits.

## ACKNOWLEDGEMENTS

We are very grateful to Statoil for funding MLB's PhD studentship and to the U.K. Natural Environment Research Council for grant NE/I027223/1 (COHBED) that enabled this research to be undertaken, using the flume facility kindly built by Bangor University technician Rob Evans. We also thank Brian Scannell, Sophie Wilmes, Ben Barton, and Nathan Howard for their help in the laboratory. Katrien Van Landeghem and Connor McCarron gave us access to the SeaTek ranging system and kindly assisted in the set-up.

## REFERENCES

- AMY, L.A., TALLING, P.J., PEAKALL, J., WYNN, R.B., AND ARZOLA THYNNE, R.G., 2005, Bed geometry used to test recognition criteria of turbidites and (sandy) debrites: *Sedimentary Geology*, v. 179, p. 163–174.
- ATKINSON, J., 2007, *The mechanics of soils and foundations*: London, CRC Press, 442 p.

963 BAAS, J.H., 2005, Sediment gravity flows: Recent advances in process and field analysis—introduction:  
 964 Sedimentary Geology, v. 179, p. 1–3.

965 BAAS, J.H., AND BEST, J.L., 2002, Turbulence modulation in clay-rich sediment-laden flows and some  
 966 implications for sediment deposition: Journal of Sedimentary Research, v. 72, p. 336–340.

967 BAAS, J.H., VAN KESTEREN, W., AND POSTMA, G., 2004, Deposits of depletive high-density turbidity  
 968 currents: A flume analogue of bed geometry, structure and texture: Sedimentology, v. 51, p. 1053–  
 969 1088.

970 BAAS, J.H., MCCAFFREY, W.D., HAUGHTON, P.D.W., AND CHOUX, C., 2005, Coupling between suspended  
 971 sediment distribution and turbulence structure in a laboratory turbidity current: Journal of  
 972 Geophysical Research: Oceans, v. 110, p. 1–20.

973 BAAS, J.H., BEST, J.L., PEAKALL, J., AND WANG, M., 2009, A phase diagram for turbulent, transitional, and  
 974 laminar clay suspension flows: Journal of Sedimentary Research, v. 79, p. 162–183.

975 BAAS, J.H., BEST, J.L., AND PEAKALL, J., 2016, Comparing the transitional behavior of kaolinite and  
 976 bentonite suspension flows: Earth Surface Processes and Landforms, v. 41, p. 1911–1921.

977 BARKER, S.P., HAUGHTON, P D.W., MCCAFFREY, W.D., ARCHER, S.G., AND HAKES, B., 2008, Development of  
 978 rheological heterogeneity in clay-rich high-density turbidity currents: Aptian Britannia Sandstone  
 979 Member, U.K. continental shelf: Journal of Sedimentary Research, v. 78, p. 45–68.

980 BLACKBOURN, G.A., AND THOMSON, M.E., 2000, Britannia Field, UK North Sea: Petrographic constraints  
 981 on Lower Cretaceous provenance, facies, and the origin of slurry-flow deposits: Petroleum  
 982 Geoscience, v. 6, p. 329–343.

983 BONNECAZE, R.T., HUPPERT, H.E., AND LISTER, J.R., 1993, Particle-driven gravity currents: Journal of Fluid  
 984 Mechanics, v. 250, p. 339–369.

985 BRITTER, R.E., AND SIMPSON, J.E., 1978, Experiments on the dynamics of a gravity current head: Journal  
 986 of Fluid Mechanics, v. 88, p. 223–240.

987 DE LEEUW, J., EGGENHUISEN, J. T., AND CARTIGNY, M. J. B., 2016, Morphodynamics of submarine channel  
 988 inception revealed by new experimental approach: Nature Communications, v. 7, 10886.

989 DROZ, L., MARSSET, T., ONDRE, H., LOPEZ, M., AND SAVOYE, B., 2003, Architecture of an active mud-rich  
990 turbidite system: The Zaire Fan (Congo-Angola margin southeast Atlantic): Results from ZaiAngo 1  
991 and 2 cruises: AAPG Bulletin, v. 87, p. 1145–1168.

992 ELVERHØI, A., ISSLER, D., DE BLASIO, F. V., ILSTAD, T., HARBITZ, C. B., AND GAUER, P., 2005, Emerging insights  
993 into the dynamics of submarine debris flows: Natural Hazards and Earth System Science, v. 5, p. 633–  
994 648.

995 FELIX, M., AND PEAKALL, J., 2006, Transformation of debris flows into turbidity currents: mechanisms  
996 inferred from laboratory experiments: Sedimentology, v. 53, p. 107–123.

997 GLADSTONE, C., PHILLIPS, J.C., & SPARKS, R.S.J, 1998, Experiments on bidisperse, constant volume gravity  
998 currents: propagation and sediment deposition: Sedimentology, v. 45, p. 833–844.

999 GRIFFIN, J.J., WINDOM, H. AND GOLDBERG, E.D., 1968, The distribution of clay minerals in the world  
1000 ocean: Deep-Sea Research, v. 15, p. 433–459.

1001 HALLWORTH, M.A., HOGG, A.J., AND HUPPERT, H.E., 1998, Effects of external flow on compositional and  
1002 particle gravity currents: Journal of Fluid Mechanics, v. 359, p. 109-142.

1003 HALLWORTH, M.A., AND HUPPERT, H.E., 1998, Abrupt transitions in high-concentrations, particle-driven  
1004 gravity currents: Physics of Fluids, v. 10, p. 1083–1087.

1005 HAMPTON, M A., 1972, The role of subaqueous debris flow in generating turbidity currents: Journal of  
1006 Sedimentary Petrology, v. 42, p. 775–793.

1007 HEALY, T., WANG, Y., AND HEALY, J.A., 2002, Muddy Coasts of the World: Processes, Deposits and  
1008 Function: Amsterdam, Elsevier, 556 p.

1009 HEEZEN, B.C., MENZIES, R.J., SCHNEIDER, E.D., EWING, W.M., AND GRANELLI, N.C.L., 1964, Congo Submarine  
1010 Canyon: AAPG Bulletin, v. 48, p. 1126-1149.

1011 HILLIER, S., 1995, Erosion, Sedimentation and Sedimentary Origin of Clays, *in* B. Velde., ed., Origin and  
1012 Mineralogy of Clays: Berlin, Springer, p. 162-219.

1013 HOLTZ, R.D., AND KOVACS, W.D., 1981, An Introduction of Geotechnical Engineering. New York, Prentice  
1014 Hall, 733 p.

1015 HUPPERT, H.E., AND SIMPSON, J.E., 1980, The slumping of gravity currents: *Journal of Fluid Mechanics*, v.  
1016 99, p. 785-799.

1017 IVERSON, R.M., 1997, *Physics of Debris Flows: Reviews of Geophysics*, v. 35, p. 245–296.

1018 JACOBSON, M.R., AND TESTIK, F.Y., 2013, On the concentration structure of high-concentration  
1019 constant-volume fluid mud gravity currents: *Physics of Fluids*, v. 25, 016602.

1020 KANE, I.A., DYKSTRA, M.L., KNELLER, B.C., TREMBLAY, S., AND MCCAFFREY, W.D., 2009, Architecture of a  
1021 coarse-grained channel-levee system: The Rosario Formation, Baja California, Mexico:  
1022 *Sedimentology*, v. 56, p. 2207–2234.

1023 KANE, I.A., MCCAFFREY, W.D., PEAKALL, J., AND KNELLER, B.C., 2010, Submarine channel levee shape and  
1024 sediment waves from physical experiments: *Sedimentary Geology*, v. 223, p. 75–85.

1025 KEEVIL, G.M., PEAKALL, J., BEST, J.L., AND AMOS, K.J., 2006, Flow structure in sinuous submarine channels:  
1026 Velocity and turbulence structure of an experimental submarine channel: *Marine Geology*, v. 229, p.  
1027 241–257.

1028 KHABBAZI BASMENJ, A., MIRJAVAN, A., GHAFOORI, M., AND CHESHOMI, A., 2016, in press, Assessment of the  
1029 adhesion potential of kaolinite and montmorillonite using a pull-out test device: *Bulletin of*  
1030 *Engineering Geology and the Environment*.

1031 KNELLER, B., AND BUCKEE, C., 2000, The structure and fluid mechanics of turbidity currents: a review of  
1032 some recent studies and their geological implications: *Sedimentology*, v. 47, p. 62–94.

1033 KOOISTRA A., VERHOEF P.N.W., BROERE W., NGAN-TILLARD D.J.M., VANTOL A.F., 1998, Appraisal of  
1034 stickiness of natural clays from laboratory tests, *in* *Proceedings of the 25th National Symposium of*  
1035 *Engineering Geology*, Delft, Netherlands, p. 101–113.

1036 KUENEN, P.H., 1951, Properties of Turbidity Currents of High Density: *Society of Economic*  
1037 *Palaeontologists and Mineralogists Special Publication*, v. 2, p. 14–33.

1038 KUENEN, P.H., AND MIGLIORINI, C.I., 1950, Turbidity Currents as a Cause of Graded Bedding: *The Journal*  
1039 *of Geology*, v. 58, p. 91–127.

1040 LAGALY, G., 1989, Principles of flow of kaolin and bentonite dispersions: *Applied Clay Science*, v. 4, p.  
1041 105–123.

- 1042 LOWE, D.R., 1982, Sediment gravity flows: II. Depositional models with special reference to high  
1043 density turbidity currents: *Journal of Sedimentary Petrology*, v. 52, p. 279–297.
- 1044 LOWE, D.R., AND GUY, M., 2000, Slurry-flow deposits in the Britannia Formation (Lower Cretaceous),  
1045 North Sea: a new perspective on the turbidity and debris flow problem: *Sedimentology*, v. 47, p. 31–  
1046 70.
- 1047 LUCKHAM, P., AND ROSSI, S., 1999, The colloidal and rheological properties of bentonite suspensions:  
1048 *Advances in Colloid and Interface Science*, v. 82, p. 43–92.
- 1049 LÜTHI, S., 1981, Experiments on non-channelized turbidity currents and their deposits: *Marine*  
1050 *Geology*, v. 40, p. 59–68.
- 1051 MARR, J. G., SHANMUGAM, G., AND PARKER, G., 2001, Experiments on subaqueous sandy gravity flows:  
1052 The role of clay and water content in flow dynamics and depositional structures: *Bulletin of the*  
1053 *Geological Society of America*, v. 113, p. 1377–1386.
- 1054 MARTINSEN, O., 1994, Mass Movements, *in* Maltman, A., ed., *The Geological Deformation of*  
1055 *Sediments*: Chapman and Hall, London, p. 127–165
- 1056 MIDDLETON, G.V., 1966, Experiments on density and turbidity currents. I, Motion of the head:  
1057 *Canadian Journal of Earth Sciences*, v. 3, p. 523–546.
- 1058 MIDDLETON, G.V., 1967, Experiments on density and turbidity currents. III, Deposition of sediment:  
1059 *Canadian Journal of Earth Sciences*, v. 4, p. 475–505.
- 1060 MIDDLETON, G., 1993, Sediment deposition from turbidity currents: *Annual Review of Earth and*  
1061 *Planetary Sciences*, v. 21, p. 89–114.
- 1062 MIDDLETON, G.V. AND HAMPTON, M.A., 1973, Sediment gravity flows: mechanics of flow and deposition,  
1063 *in* Middleton, G.V., and Bouma, A.H., eds., *Turbidites and Deep Water Sedimentation*: SEPM, Pacific  
1064 Coast Section, Short Course, Anaheim, California, p. 1–38
- 1065 MIDDLETON, G.V. AND NEAL, W.J., 1989, Experiments on the thickness of beds deposited by turbidity  
1066 currents: *Journal of Sedimentary Petrology*, v. 59, p. 297–307.

1067 MOHRIG, D., AND MARR, J.G., 2003, Constraining the efficiency of turbidity current generation from  
 1068 submarine debris flows and slides using laboratory experiments: *Marine and Petroleum Geology*, v.  
 1069 20, p. 883–899.

1070 MOHRIG, D., WHIPPLE, K.X., HONDZO, M., ELLIS, C., AND PARKER, G., 1998, Hydroplaning of subaqueous  
 1071 debris flows: *Bulletin of the Geological Society of America*, v. 110, p. 387–394.

1072 MULDER, T., AND ALEXANDER, J., 2001, The physical character of subaqueous sedimentary density flow  
 1073 and their deposits: *Sedimentology*, v. 48, p. 269–299.

1074 MULDER, T., SAVOYE, B., AND SYVITSKI, J.P M., 1997, Numerical modelling of a mid-sized gravity flow: The  
 1075 1979 Nice turbidity current (dynamics, processes, sediment budget and seafloor impact):  
 1076 *Sedimentology*, v. 44, p. 305–326.

1077 MUTTI, E., TINTERRI, R., REMACHA, E., MAVILLA, N., ANGELLA, S., AND FAVA, L., 1999, An introduction to the  
 1078 analysis of ancient turbidite basins from an outcrop perspective: *American Association of Petroleum*  
 1079 *Geologists, Continuing Education Course Note Series*, v. 39, 96 p.

1080 PARKER, G., GARCIA, M., FUKUSHIMA, Y., AND YU, W., 1987, Experiments on turbidity currents over an  
 1081 erodible bed: *Journal of Hydraulic Research*, v. 25, p. 123–147.

1082 PASHLEY, R., AND KARAMAN, M., 2004, *Applied colloid and surface chemistry*: London, Wiley, 200 p.

1083 SALAHELDIN, T.M., IMRAN, J., CHAUDHRY, M.H., AND REED, C., 2000, Role of fine-grained sediment in  
 1084 turbidity current flow dynamics and resulting deposits: *Marine Geology*, v. 171, p. 21-38.

1085 SCHINDLER, R.J., PARSONS, D.R., YE, L., HOPE, J.A., BAAS, J.H., PEAKALL, J., MANNING, A.J., ASPDEN,  
 1086 R.J., MALARKEY, J., SIMMONS, S., PATERSON, D.M., LICHTMAN, I.D., DAVIES, A.G., THORNE, P.D. AND BASS, S.J.,  
 1087 2015, Sticky stuff: Redefining bedform prediction in modern and ancient environments: *Geology*, v.  
 1088 43, p. 399–402.

1089 SUMNER, E.J., AND PAULL, C.K., 2014, Swept away by a turbidity current in Mendocino submarine  
 1090 canyon, California: *Geophysical Research Letters*, v. 41, p. 7611–7618.

1091 SUMNER, E.J., TALLING, P.J., AND AMY, L. A., 2009, Deposits of flows transitional between turbidity  
 1092 current and debris flow: *Geology*, v. 37, p. 991–994.

1093 TALLING, P.J., 2013, Hybrid submarine flows comprising turbidity current and cohesive debris flow:  
 1094 Deposits, theoretical and experimental analyses, and generalized models: *Geosphere*, v. 9, p. 460–  
 1095 488.

1096 TALLING, P.J., AMY, L.A., WYNN, R.B., PEAKALL, J., AND ROBINSON, M., 2004, Beds comprising debrite  
 1097 sandwiched within co-genetic turbidite: Origin and widespread occurrence in distal depositional  
 1098 environments: *Sedimentology*, v. 51, p. 163-194.

1099 TALLING, P.J., WYNN, R.B., MASSON, D.G., FRENZ, M., CRONIN, B.T., SCHIEBEL, R., AKHMETZHANOV,  
 1100 A.M., DALLMEIER-TIESSEN, S., BENETTI, S., WEAVER, P.P.E., GEORGIOPOULOU, A., ZÜHLSORFF, C. AND AMY,  
 1101 L.A., 2007, Onset of submarine debris flow deposition far from original giant landslide: *Nature*, v.  
 1102 450, p. 541–544.

1103 TALLING, P.J., PAULL, C.K., AND PIPER, D.J.W., 2013, How are subaqueous sediment density flows  
 1104 triggered, what is their internal structure and how does it evolve? Direct observations from  
 1105 monitoring of active flows: *Earth-Science Reviews*, v. 125, p. 244–287.

1106 TALLING, P.J., ALLIN, J., ARMITAGE, D.A., ARNOTT, R.W.C., CARTIGNY, M.J.B., CLARE, M.A., FELLETTI, F.,  
 1107 COVAULT, J. A., GIRARD-CLOS, S., HANSEN, E., HILL, P.R., HISCOTT, R.N., HOGG, A.J., CLARKE, J.H., JOBE, Z.R.,  
 1108 MALGESINI, G., MOZZATO, A., NARUSE, H., PARKINSON, S., PEEL, F.J., PIPER, D.J.W., POPE, E., POSTMA, G.,  
 1109 ROWLEY, P., SGUAZZINI, A., STEVENSON, C.J., SUMNER, E.J., SYLVESTER, Z., WATTS, C., AND XU, J., 2015, Key  
 1110 future directions for research on turbidity currents and their deposits: *Journal of Sedimentary*  
 1111 *Research*, v. 85, p. 153-169.

1112 TAN, X., HU, L., REED, A. H., FURUKAWA, Y., AND ZHANG, G, 2014, Flocculation and particle size analysis of  
 1113 expansive clay sediments affected by biological, chemical, and hydrodynamic factors: *Ocean*  
 1114 *Dynamics*, v. 64, p. 143–157.

1115 VAN VLIET, T., 2013, *Rheology and fracture mechanics of foods*: London, CRC Press, 363 p.

1116 WANG, Z., AND PLATE, E.C.H.J., 1996, A preliminary study on the turbulence structure of flows of non-  
 1117 Newtonian fluid: *Journal of Hydraulic Research*, v. 34, p. 345–361.

1118 VAN WEERING, T.C. E., AND VAN IPEREN J., 1984, Fine-grained sediments of the Zaire deep-sea fan,  
 1119 southern Atlantic Ocean, *in* Stow D. A. V., and Piper D. J. W., eds., *Fine-grained sediments: deep-*  
 1120 *water processes and facies*: Geological Society Special Publication 15, p. 95–113

- 1121 WILSON, D., DAVIES, J., WALTERS, R., AND ZALASIEWICZ, J., 1992, A fault-controlled depositional model for  
1122 the Aberystwyth Grits turbidite system: *Geological Magazine*, v. 129, p. 595–607.
- 1123 WINDOM, H.L., 1976, Lithogeneous material in marine sediments, *in* Riley, J.P., Chester, R., eds.,  
1124 *Chemical Oceanography*, Vol. 5: New York, Academic Press, pp. 103–135
- 1125 WINTERWERP, J.C., AND VAN KESTEREN, W.G.M., 2004. Introduction to the Physics of Cohesive Sediment  
1126 in the Marine Environment: Oxford, U.K., Elsevier, *Developments in Sedimentology* 56, 559 p.
- 1127 XU, J., 2011, Measuring currents in submarine canyons: Technological and scientific progress in the  
1128 past 30 years: *Geosphere*, v. 7, p. 868–876.
- 1129 XU, J.P., SEQUEIROS, O.E., AND NOBLE, M.A., 2014, Sediment concentrations, flow conditions, and  
1130 downstream evolution of two turbidity currents, Monterey Canyon, USA: *Deep-Sea Research Part I*  
1131 *Oceanographic Research Papers*, v. 89, p. 11–34.
- 1132 YONG, R.N., NAKANO, M., AND PUSCH, R., 2012, *Environmental Soil Properties and Behavior*. London,  
1133 CRC Press, 455p.

## 1134 **FIGURE CAPTIONS**

1135 **Figure 1:** Experimental setup. HD = high-definition.

1136 **Figure 2:** Video snapshot of the (A) fully turbulent 5% silica flour flow at  $t = 8.00$  s and at  $x = 1.80$  m  
1137 along the tank; (B) Head of the 25% silica flour flow, which was also turbulence-dominated, at  $t =$   
1138  $1.70$  s and  $x = 0.90$  m; (C) Two-layer structure of the HDTC laden with 48% silica flour at  $t = 3.40$  s  
1139 and  $x = 1.80$  m; (D) Final stages of the 52% silica flour slide at  $t = 7.44$  s and  $x = 0.55$  m. Length of  
1140 scale bar is 25 mm.

1141 **Figure 3:** Changes in the head velocity of the silica flour flows with (A)  $1\% \leq C \leq 44\%$ , and (B)  $46\% \leq C$   
1142  $\leq 52\%$ , along the length of the lock-exchange tank. The red, blue, green, and black colors indicate  
1143 low-density turbidity currents, high-density turbidity currents, non-cohesive mud flow, and slide,  
1144 respectively.

1145 **Figure 4:** Deposit thickness against distance along the tank for all silica flour flows with measurable  
1146 run-out distance. See Fig. 3 for explanation of line colors.

1147 **Figure 5:** (A) Head of the 22% kaolinite flow at  $t = 3.50$  s and  $x = 1.50$  m; this HDTC hydroplaned and  
1148 was divided into three parts; the arrows highlight the FES; (B) Rounded head of the hydroplaning

25% kaolinite-laden HDTC at  $t = 2.36$  s and  $x = 0.87$  m; (C) Pointed head of the mud flow with  $C = 27\%$  at  $t = 3.50$  s and  $x = 0.89$  m; small tension cracks, shown by the arrows, are visible on the top of the head of the flow; (D) Rounded head of the slide with  $C = 29\%$  at  $t = 2.50$  s and  $x = 0.35$  m. Length of scale bar is 25 mm.

**Figure 6:** Changes in the head velocity of the kaolinite flows with (A)  $1\% \leq C \leq 15\%$ , and (B)  $22\% \leq C \leq 29\%$ , along the length of the lock-exchange tank. See Fig. 3 for explanation of line colors.

**Figure 7:** Deposit thickness against distance along the tank for all kaolinite flows with measurable run-out distance. See Fig. 3 for explanation of line colors.

**Figure 8:** (A) Tripartite head of the 16% bentonite flow at  $t = 6.07$  s and  $x = 1.77$  m; a cohesive packet of clay is visible at the base of the head of this HDTC; the arrow highlights a FES; (B) Head of the 17% bentonite flow at  $t = 5.40$  s and  $x = 1.49$  m; the horizontal sheets and angled FES are shown by the dashed and solid arrows, respectively; (C) Mud flow laden with 19% bentonite, showing a folded head, at  $t = 2.73$  s and  $x = 0.56$  m; (D) Front of the 20% bentonite slide at  $t = 5.43$  s and  $x = 0.13$  m. Length of scale bar is 25 mm.

**Figure 9:** Changes in the head velocity of the bentonite flows with (A)  $1\% \leq C \leq 15\%$ , and (B)  $16\% \leq C \leq 20\%$ , along the length of the lock-exchange tank. See Fig. 3 for explanation of line colors. Blue dashed line in (A) denotes extrapolated velocity to the recorded run-out distance.

**Figure 10:** Deposit thickness against distance along the tank for all bentonite flows with measurable run-out distance. See Fig. 3 for explanation of line colors. Dashed end of the deposit for the 15% flow was beyond the reach of the SEATEK ranging system, and was measured by hand instead.

**Figure 11:** (A) Maximum head velocity and (B) deposit run-out distance against suspended sediment concentration for the three sediment types.

**Figure 12:** Non-dimensional relationship between  $C$  and  $U_h$  for the kaolinite, bentonite, and silica flour flows. Dots represent experimental data. Solid lines denote best-fit curves (Equations 1a, b).

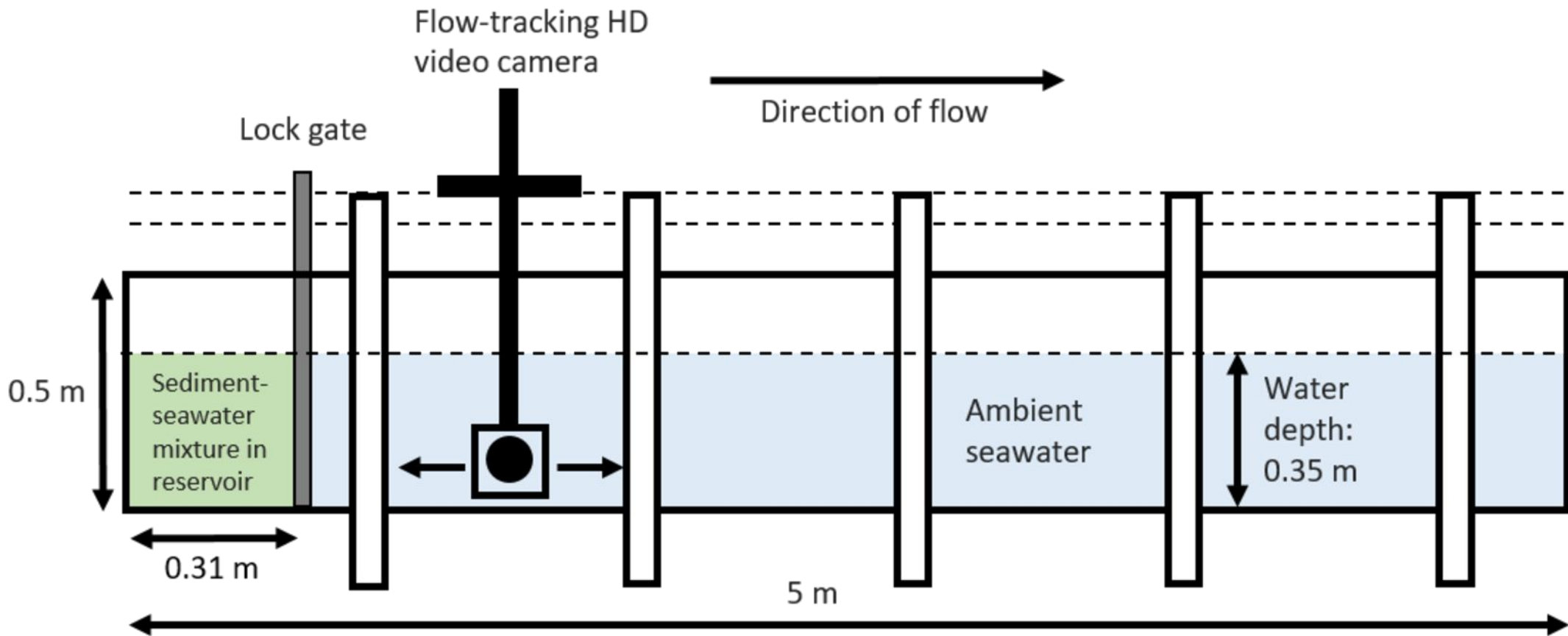
**Figure 13:** (A)  $C/C_m$  against yield stress for bentonite and kaolinite. (B)  $(C - C_m)/(C_0 - C_m)$  against yield stress for bentonite and kaolinite. Dots represent experimental data. Solid lines denote best-fit curves (Equations 3a, b).

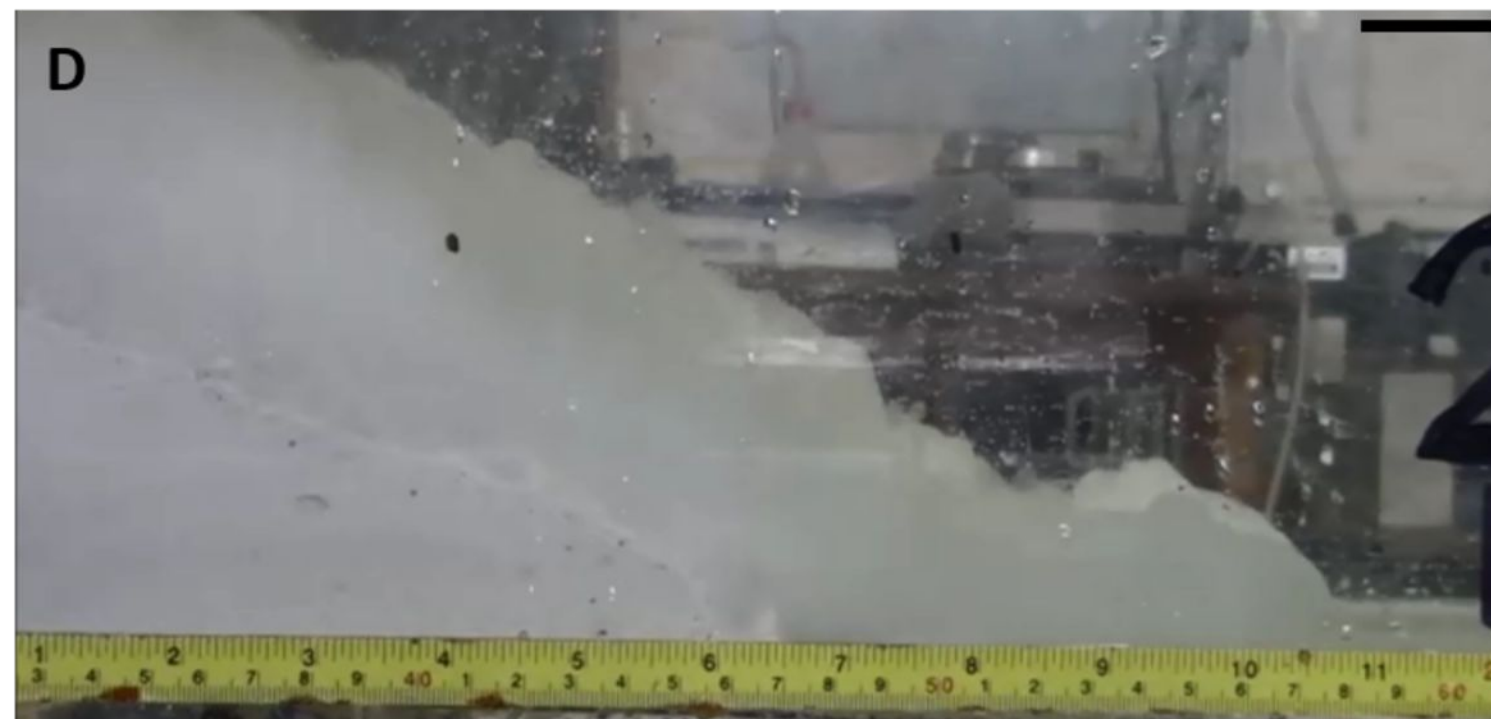
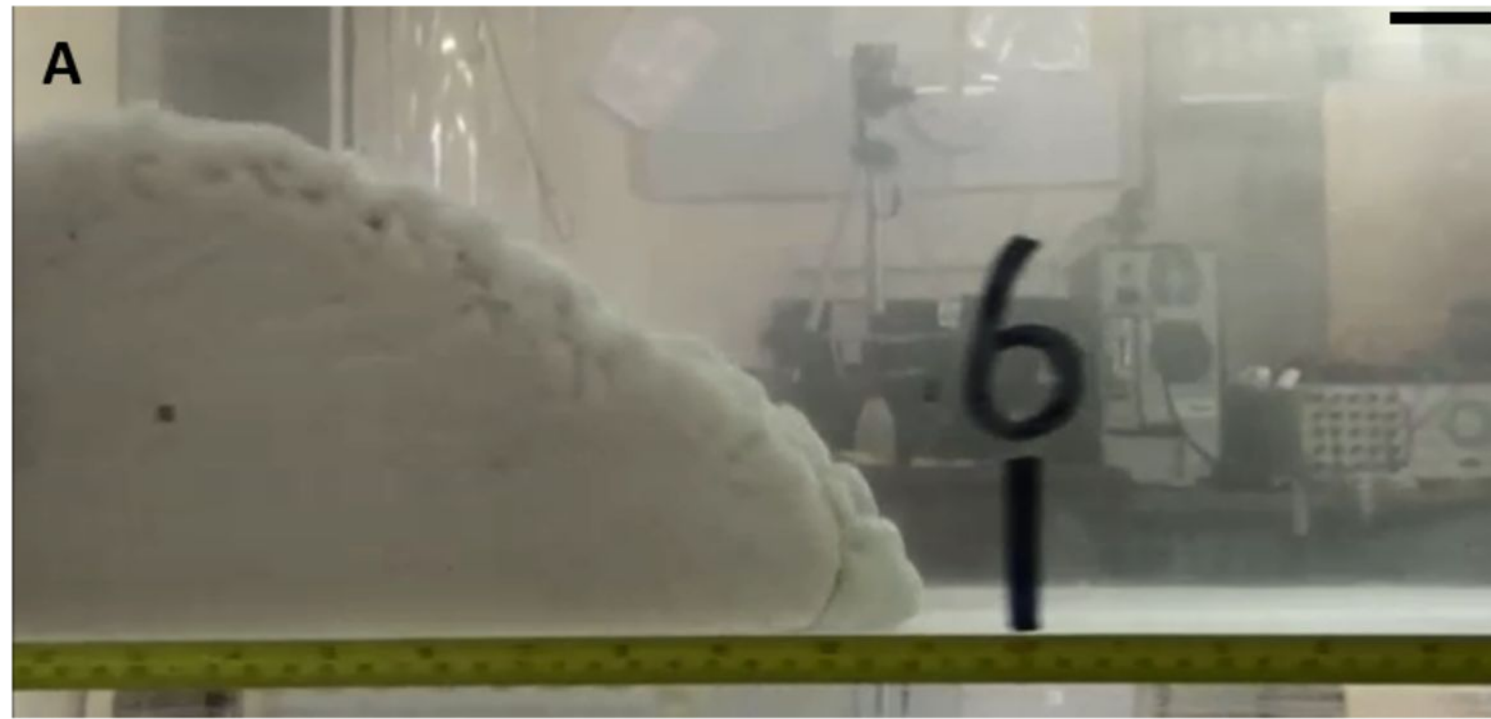
**Figure 14:**  $U_h/U_{h,m}$  against yield stress for kaolinite and bentonite. Dots represent experimental data. Solid line denotes best-fit curve (Equations 4a, b). LDTC = low-density turbidity current; HDTC = high-

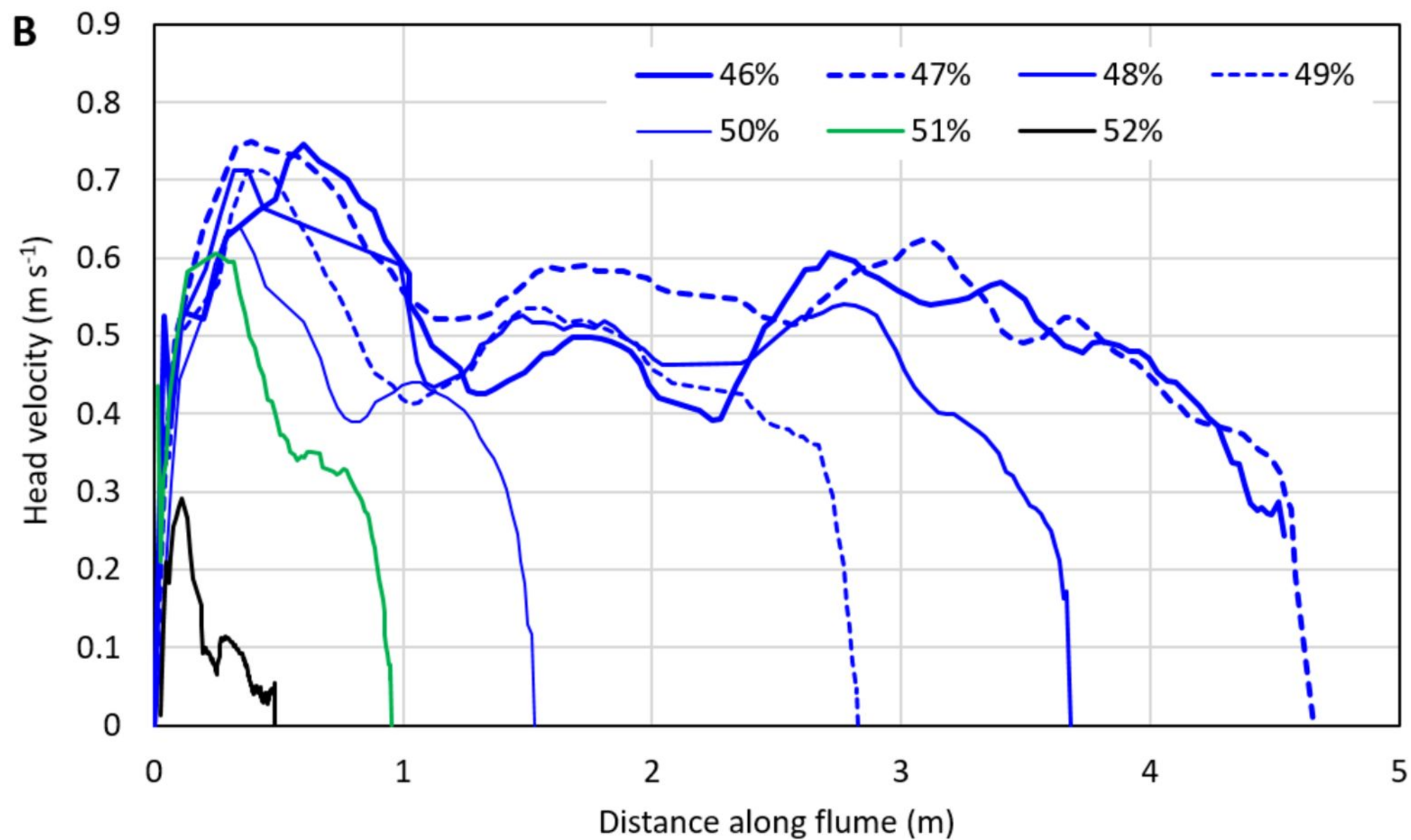
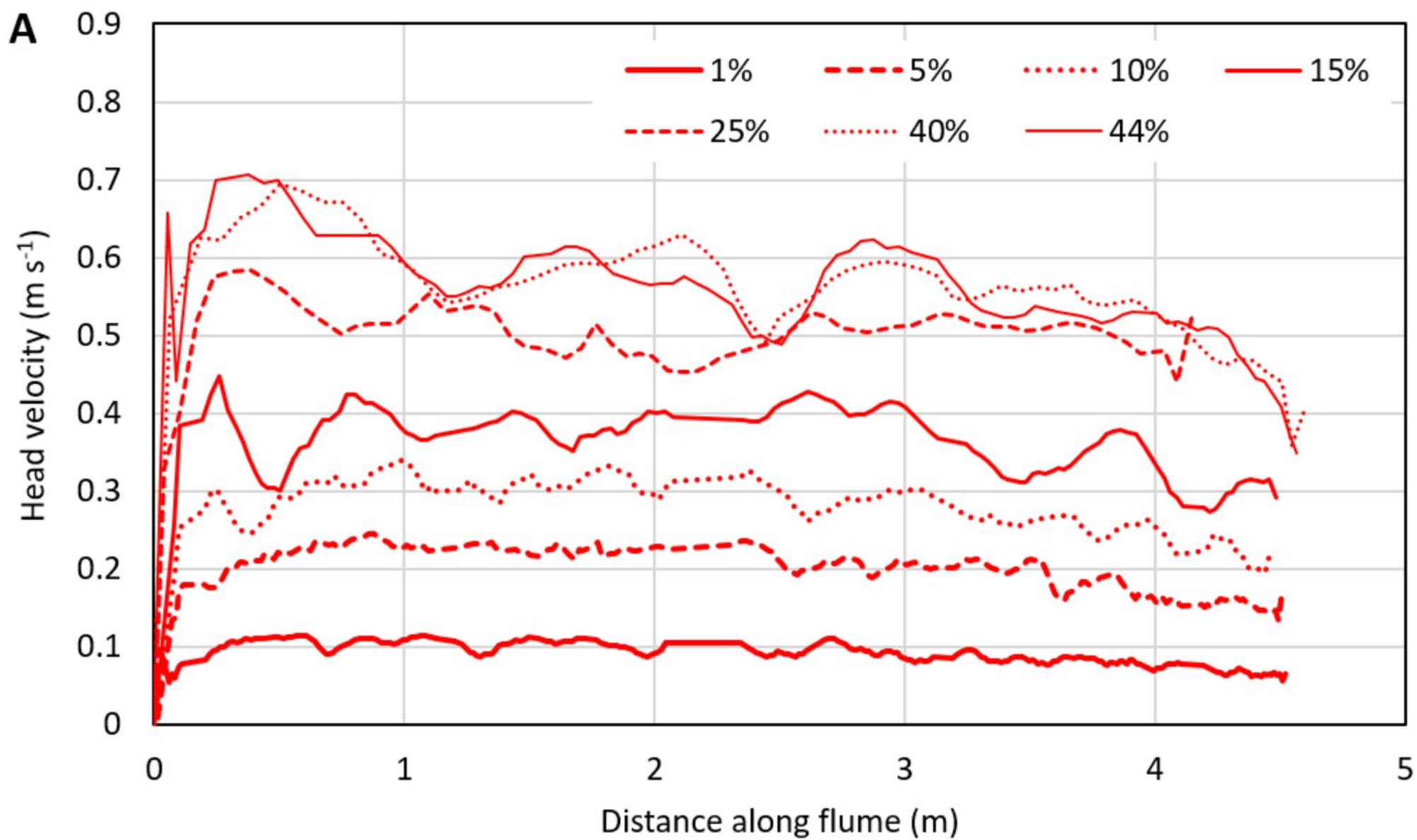
density turbidity current; CMF = cohesive mud flow. Boundaries between flow types are average yield stress values based on the ranges in Table 3.

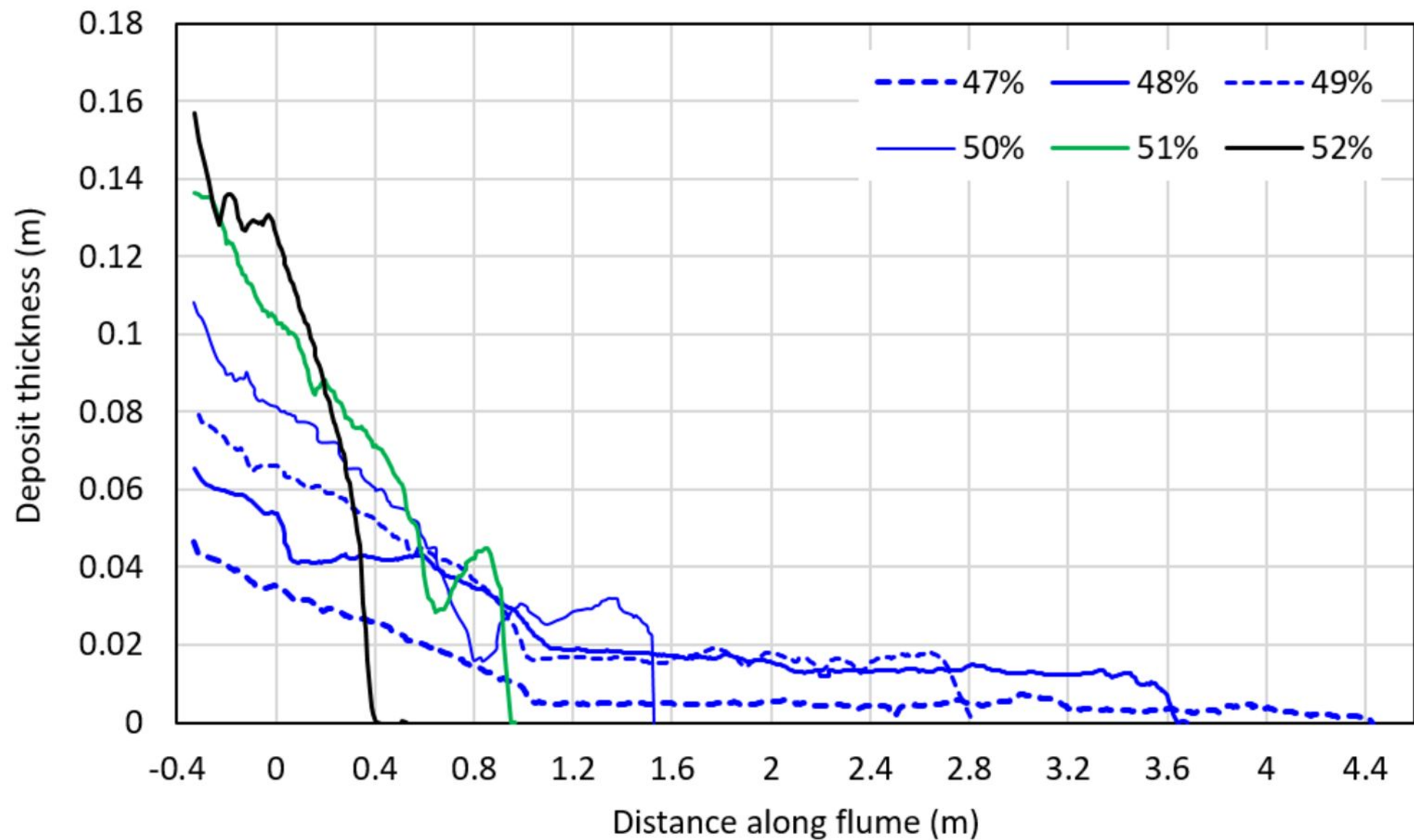
**Figure 15:** (A) Run-out distance,  $x_0$ , against dimensionless concentration,  $C/C_0$  for all flows. Dots represent experimental data. Solid lines represent fit to the data (Equation 6b), and dashed lines represent predictions by Hallworth and Huppert (1998) for low-concentration flows (Equation 5) The cross-over between these lines denotes the predicted maximum run-out distance,  $x_{0,m}$ . (B) fit of  $x_0/x_{0,m}$  to  $(C-C_m)/(C_0-C_m)$  for all the experiment data.

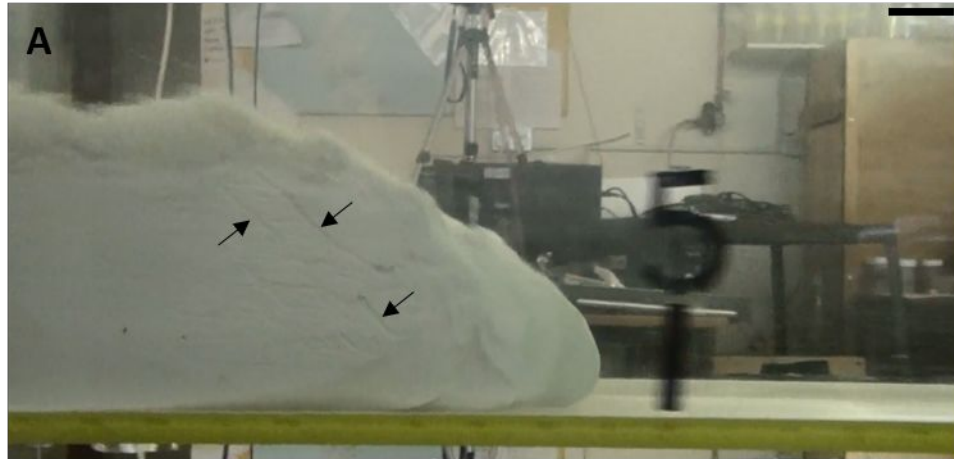
**Figure 16:** Dimensionless run-out distances of the clay flows, or deposit length, against yield stress for kaolinite and bentonite. Dots represent experimental data. Solid lines denote curves according to Equation 8. LDTC = low-density turbidity current; HDTC = high-density turbidity current; CMF = cohesive mud flow. Boundaries between flow types are average yield stress values based on the ranges in Table 3.

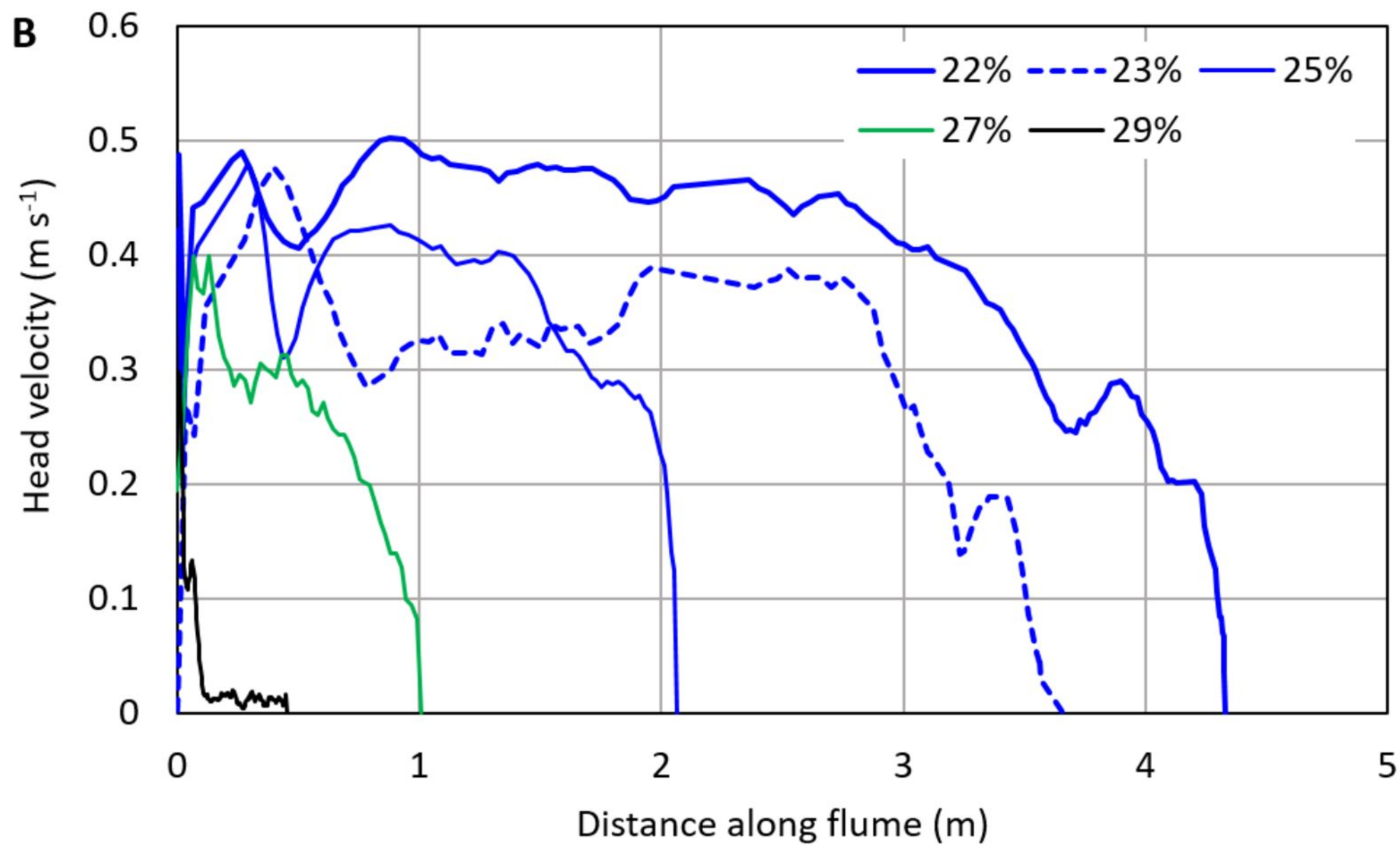
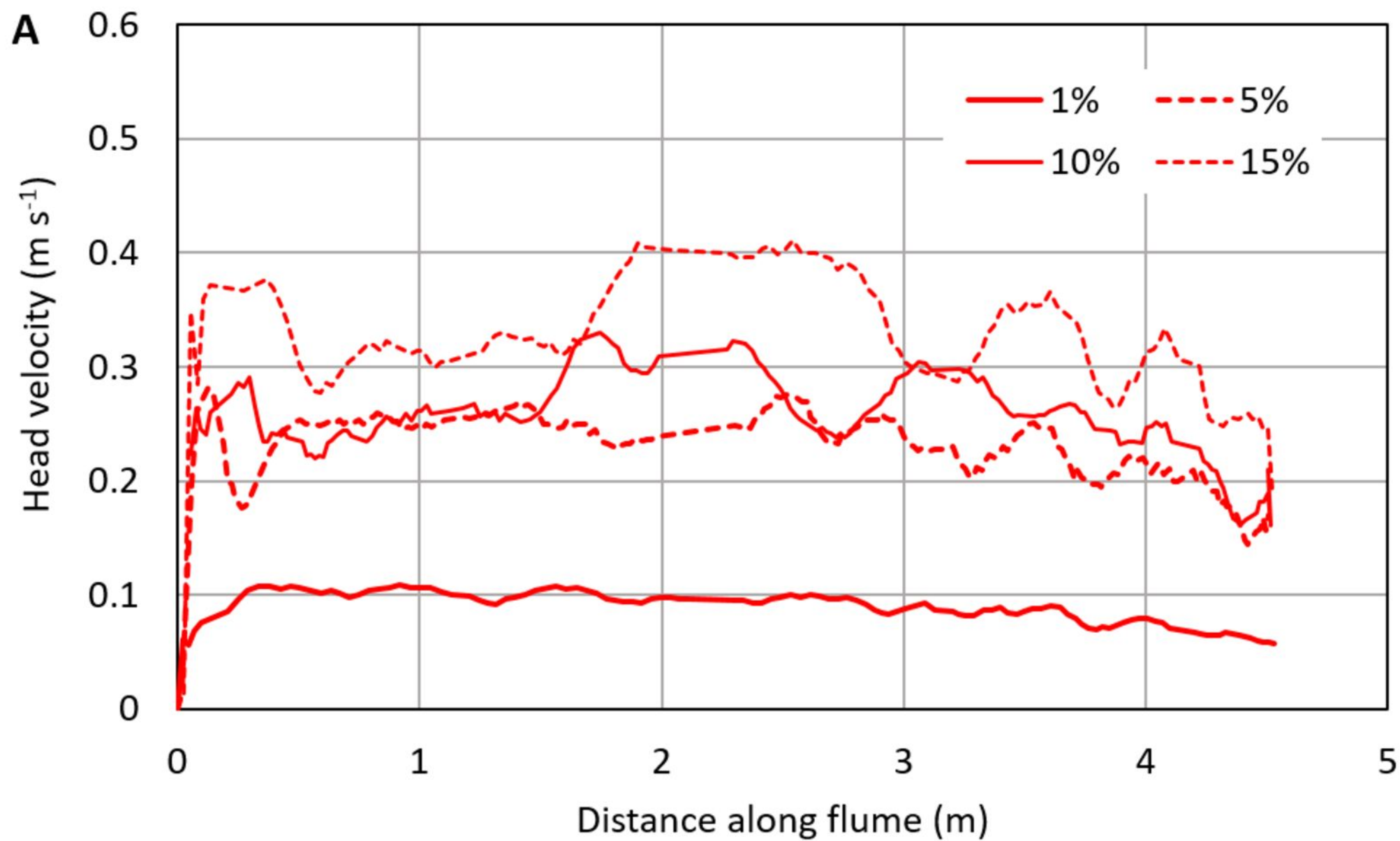


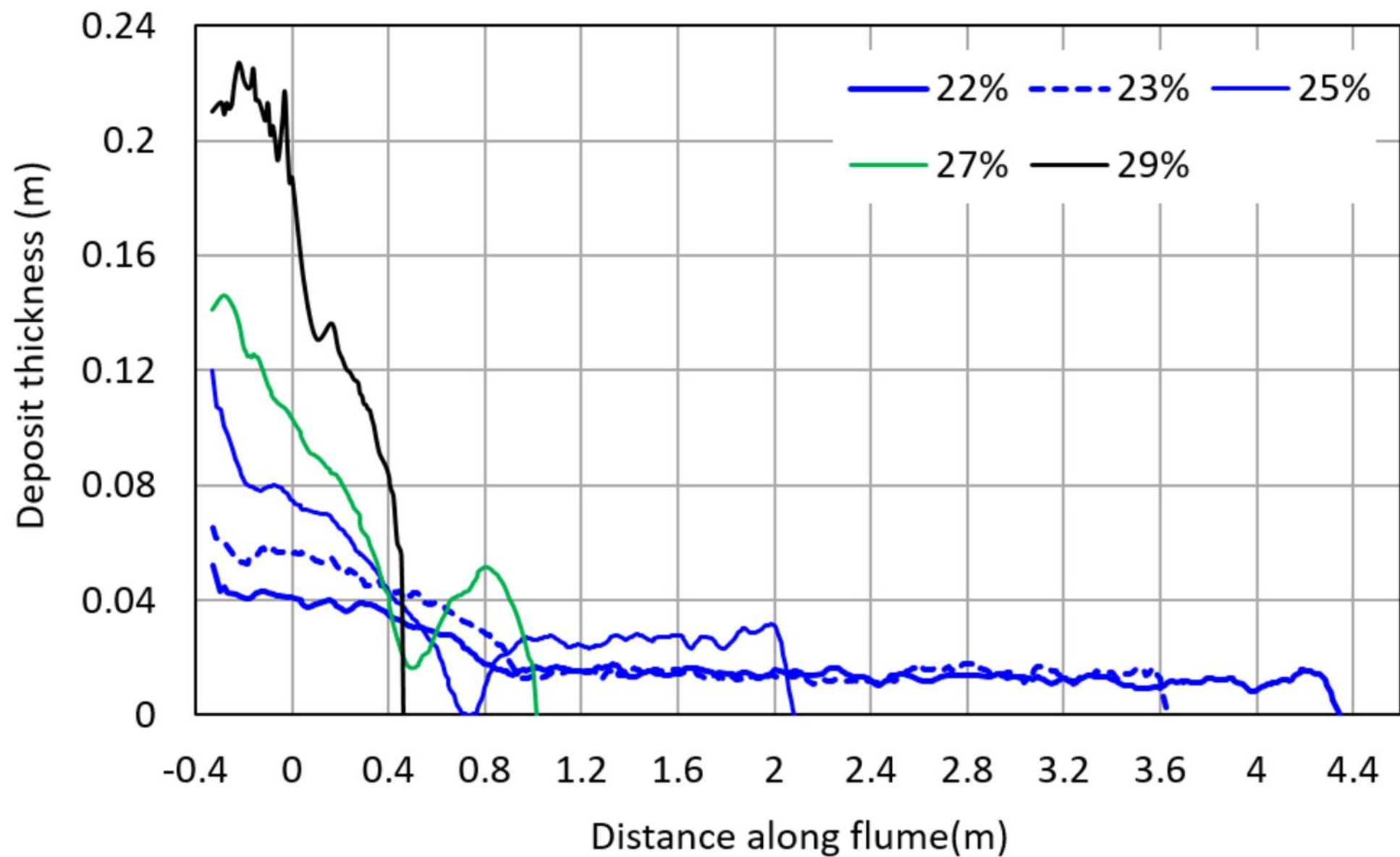


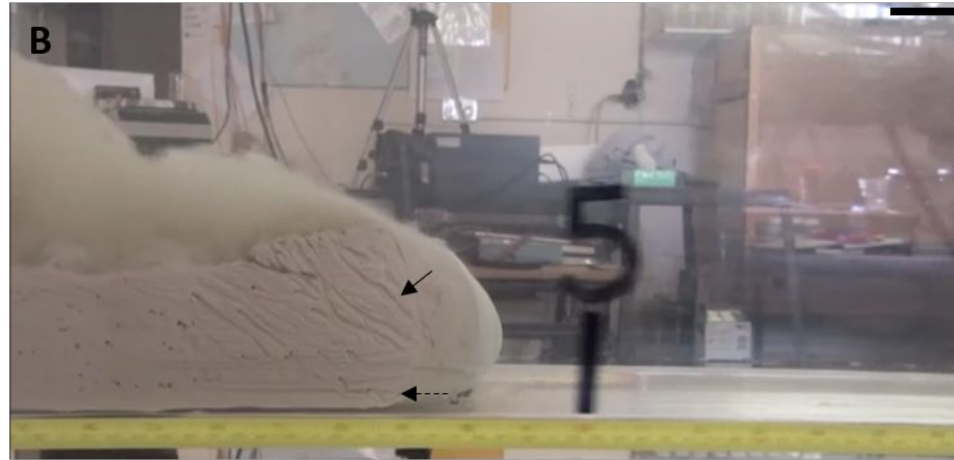


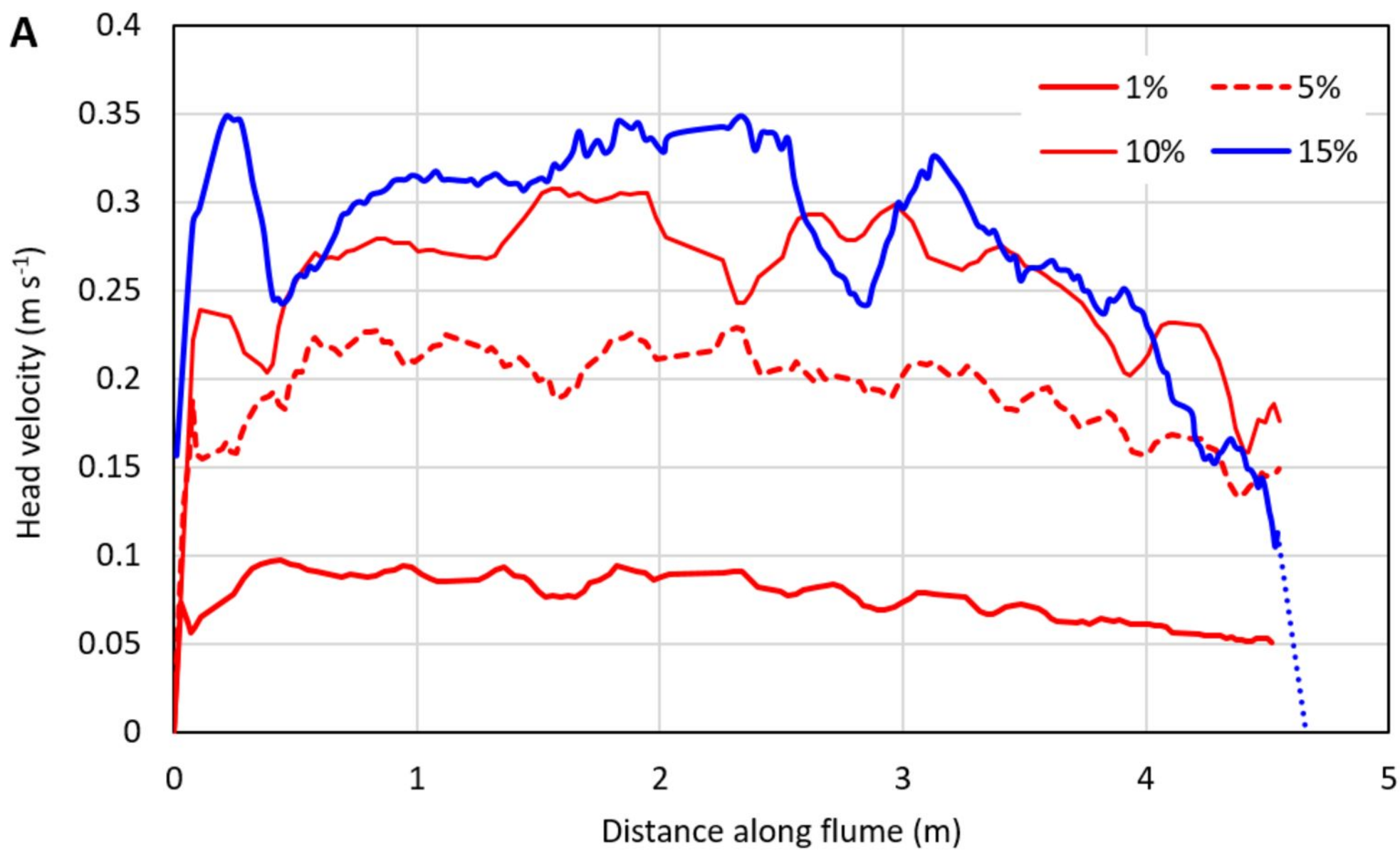
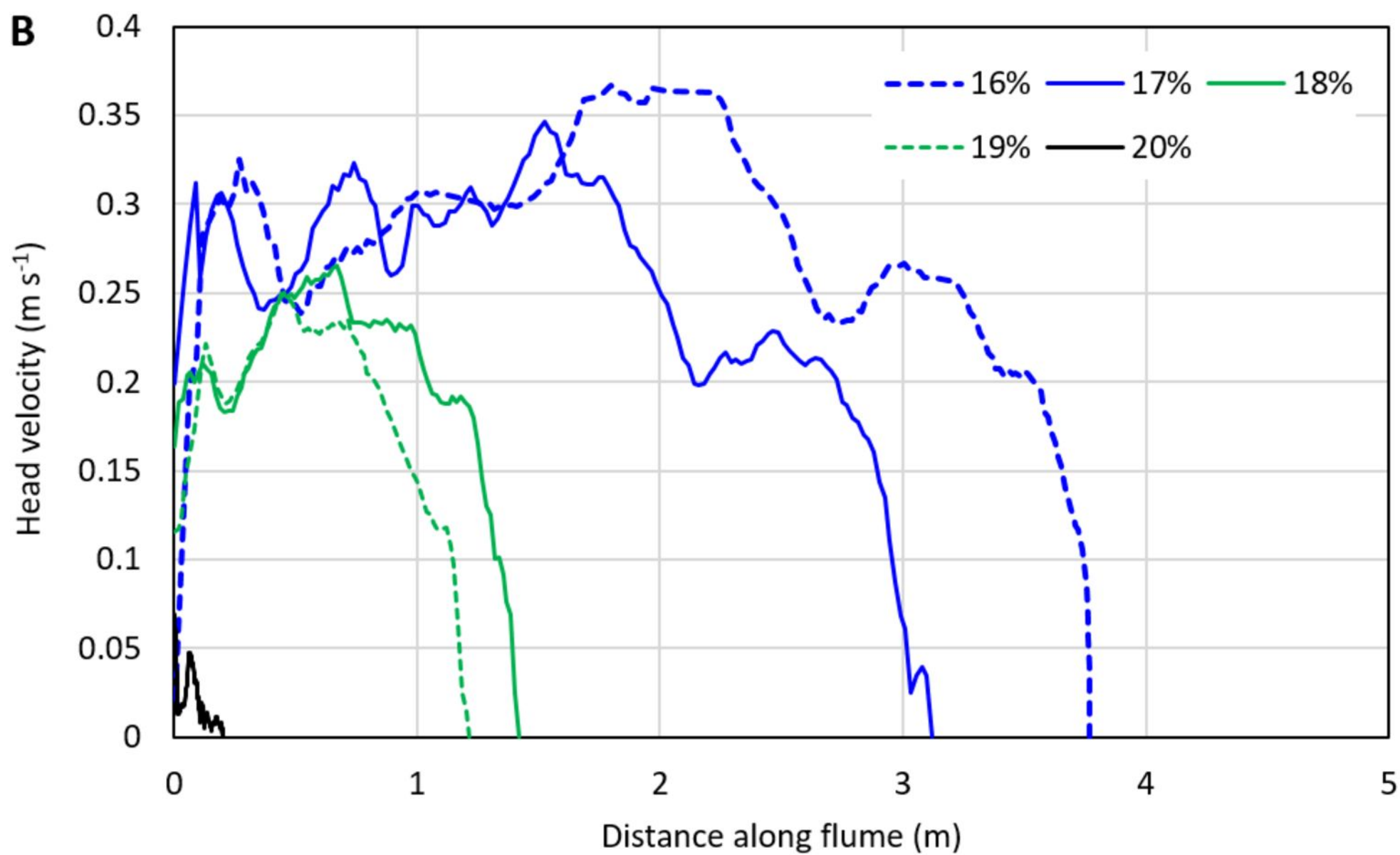


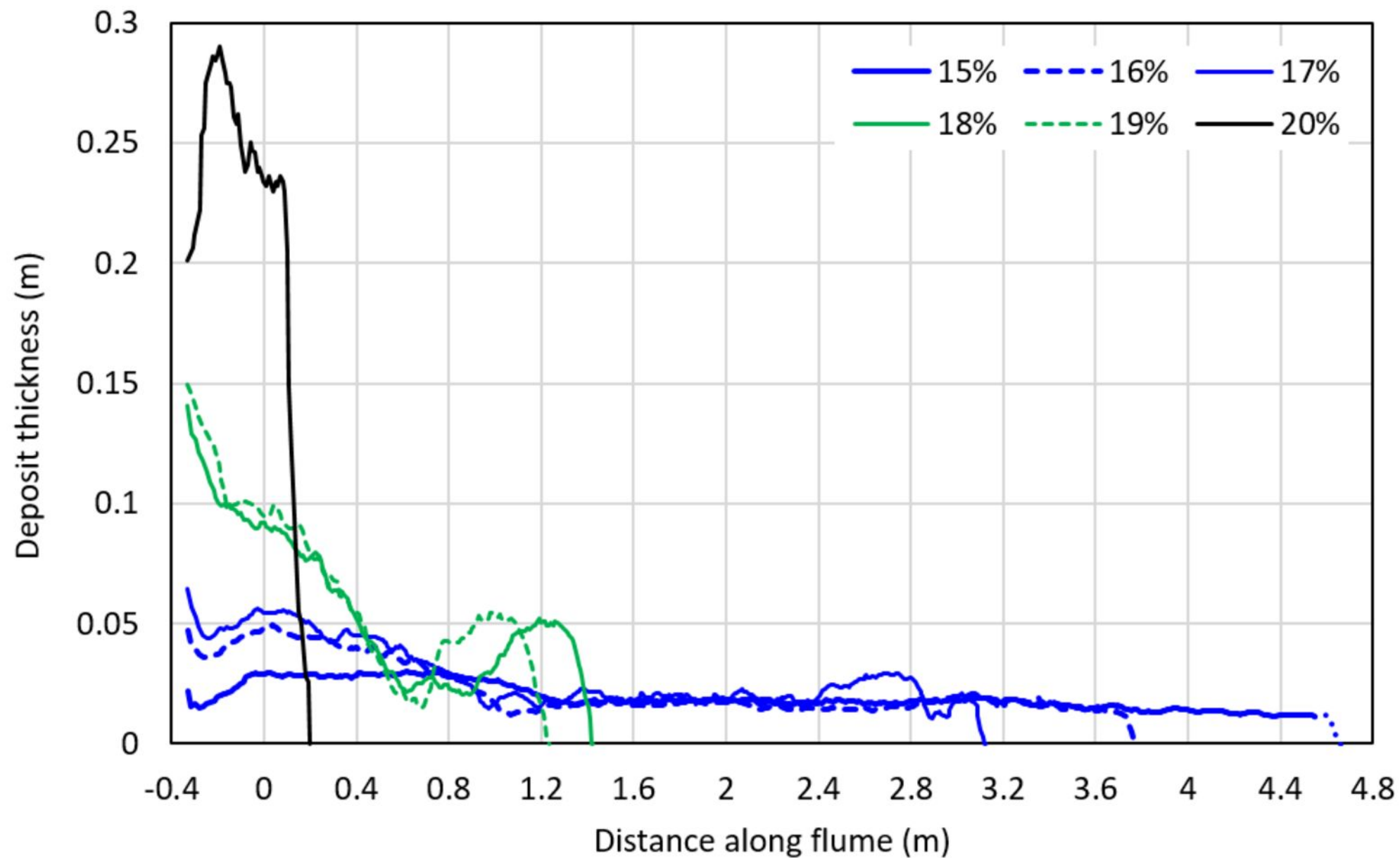


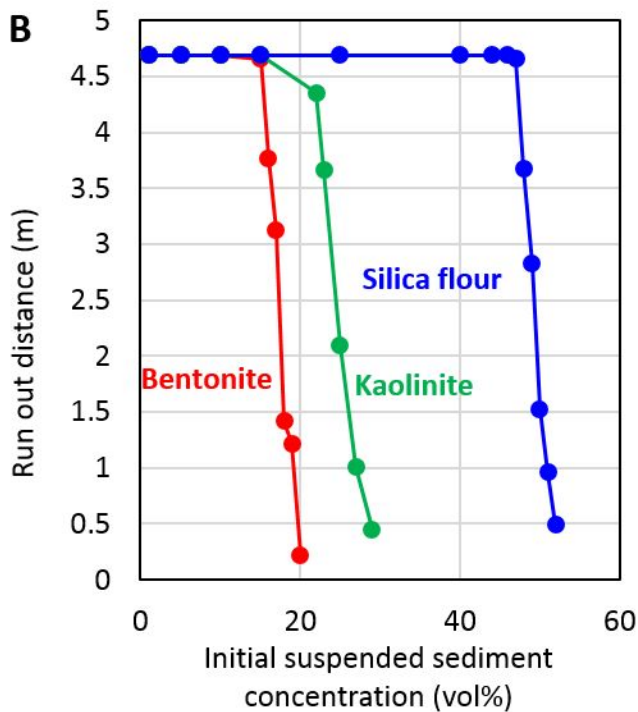
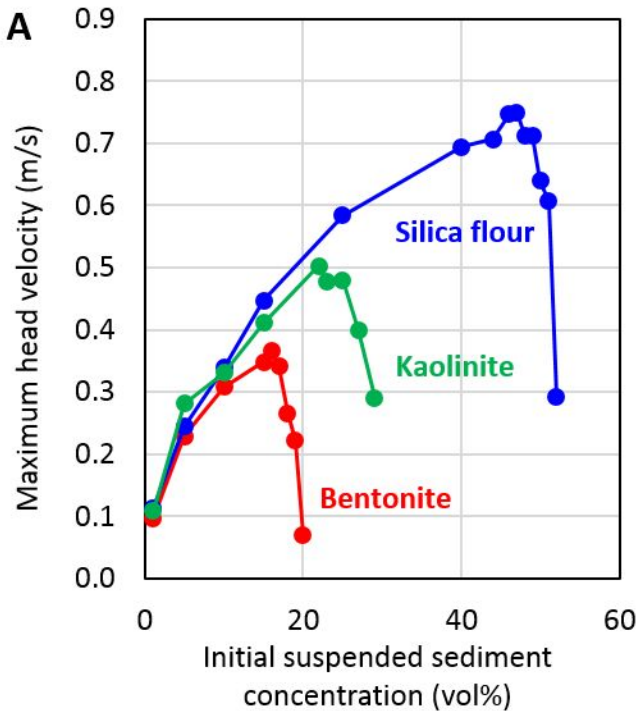


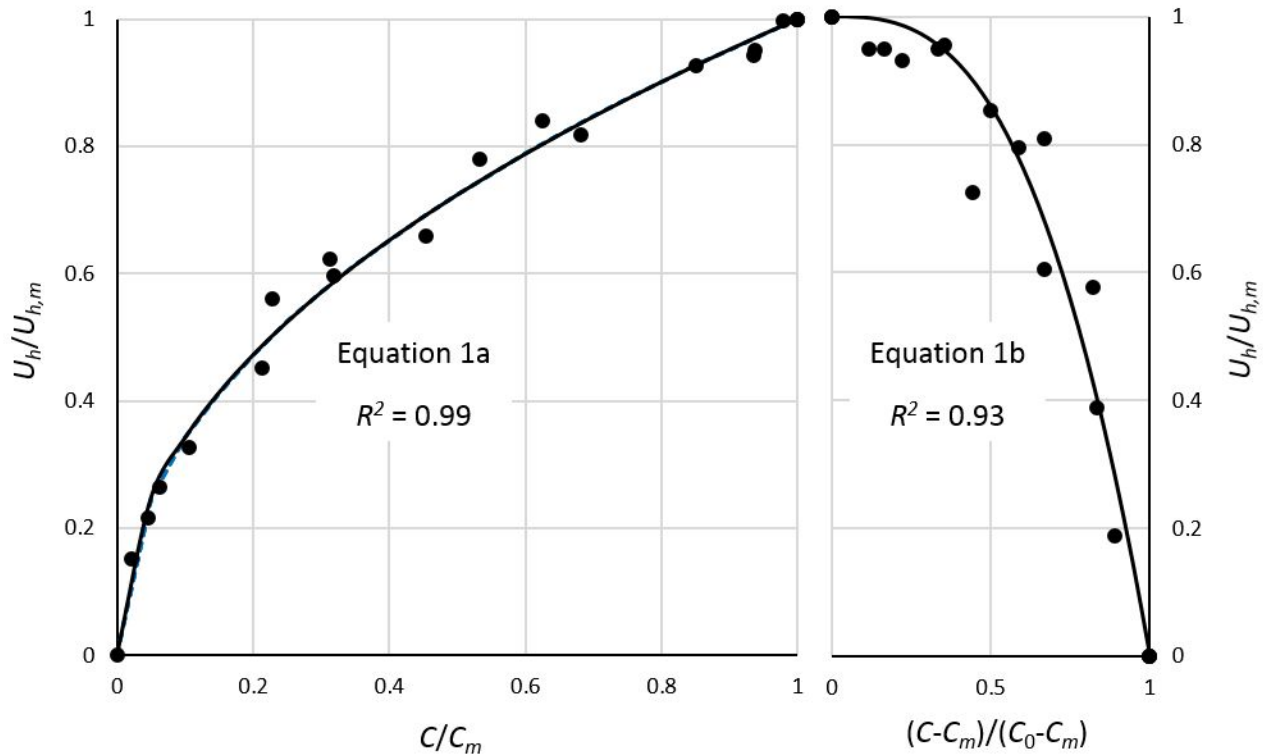


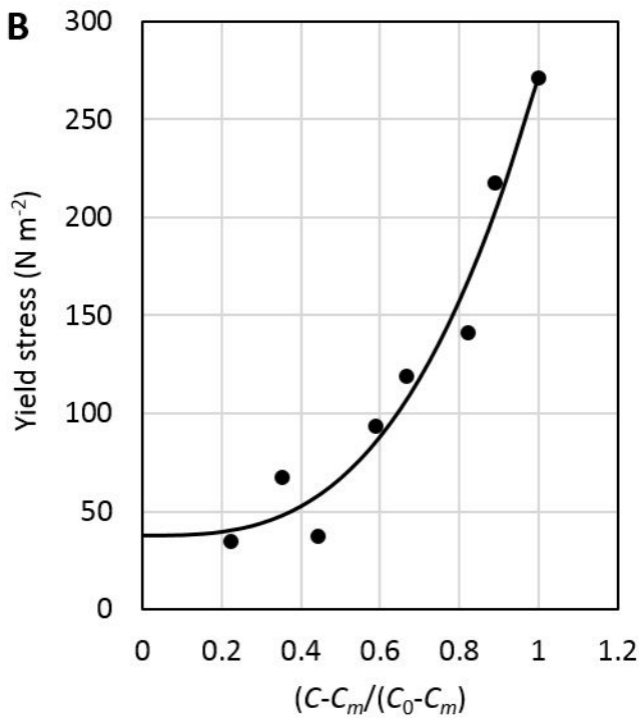
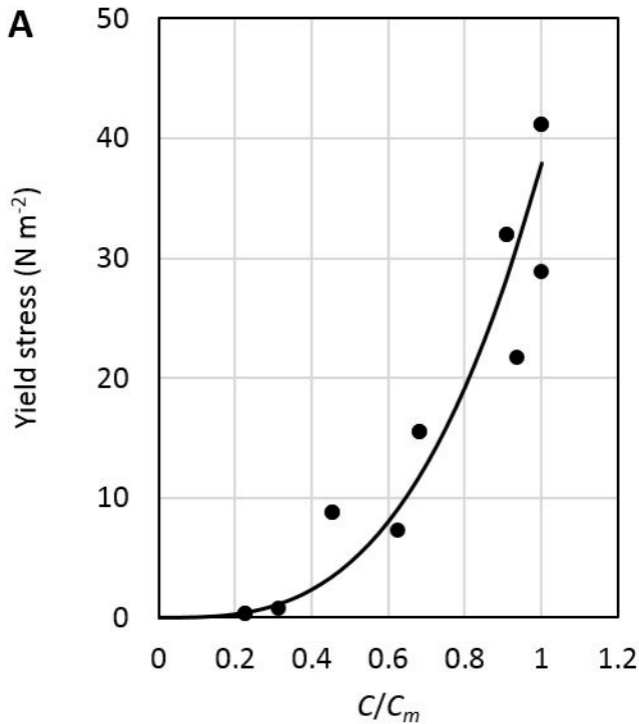


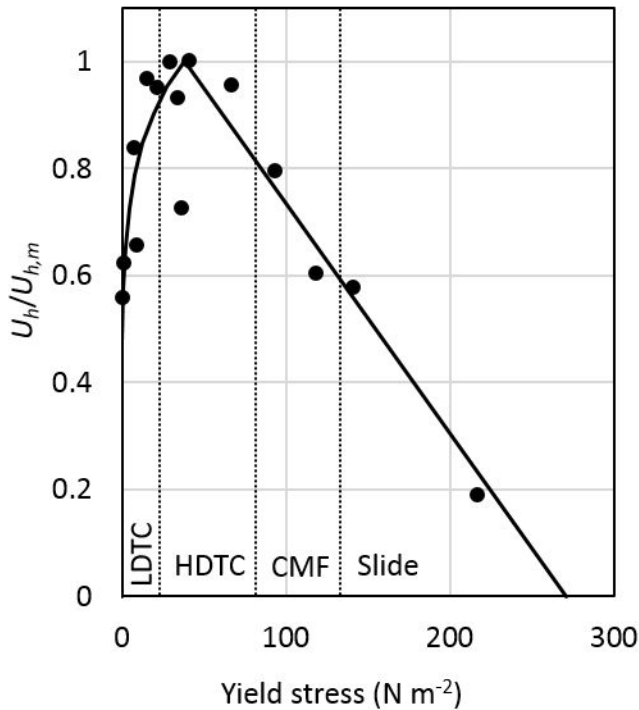
**A****B**

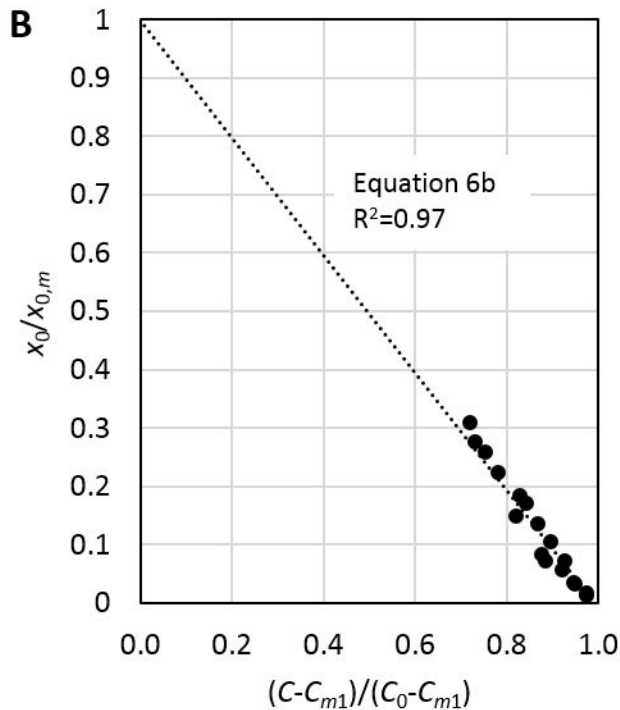
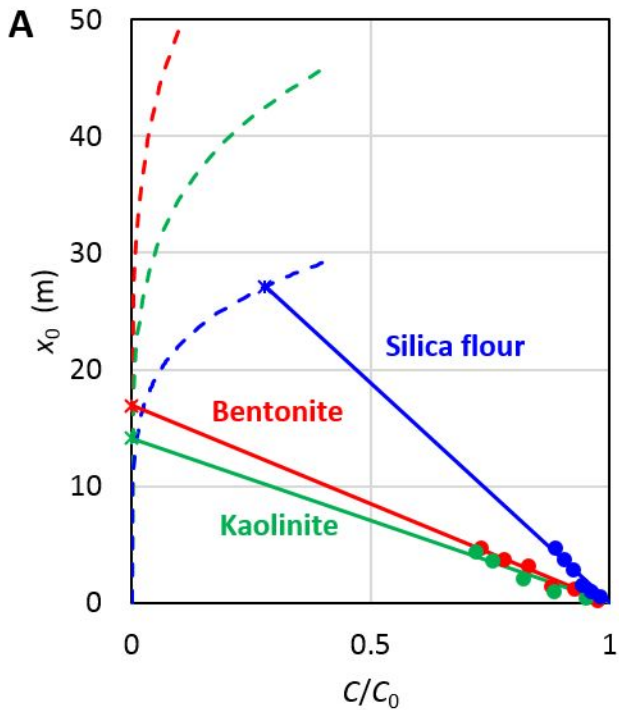


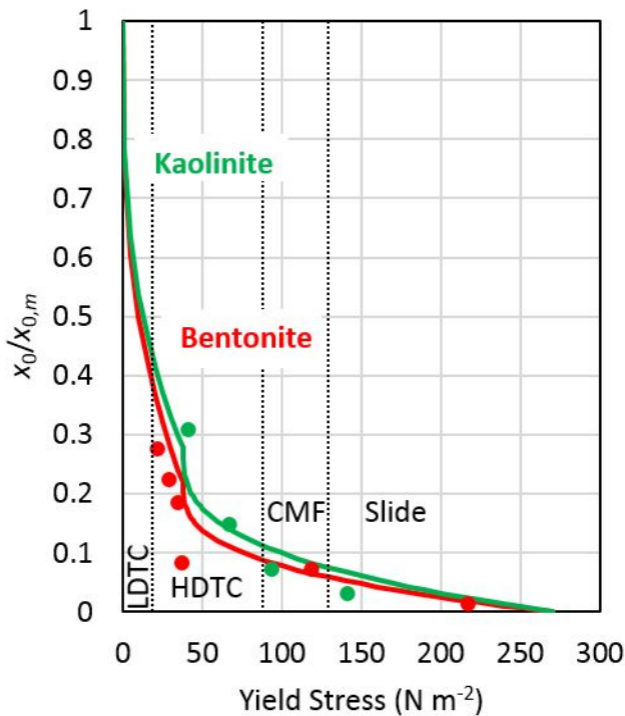













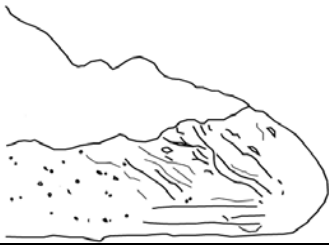


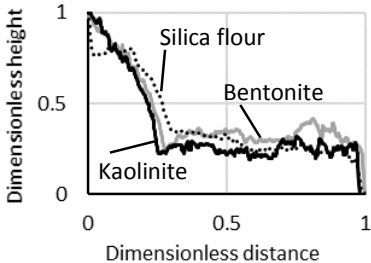
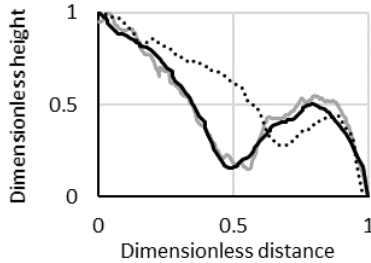
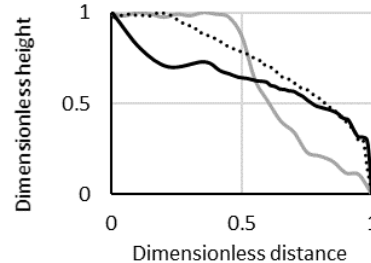
**Table 1:** Typical values of thickness, size, specific surface area, and cation exchange capacity of common clay minerals. Bentonite is part of the montmorillonite group of clay minerals. The clay minerals are sorted from small to large. Modified after Hillel (2003) and Yong et al. (2012).

Edge view	Typical thickness (nm)	Planar diameter (nm)	Specific surface area (SSA) (m <sup>2</sup> /kg)	Cation exchange capacity (CEC) (mEq/100g)
<b>Montmorillonite (Incl. Bentonite)</b>	2	10-1,000	700-800	80-100
<b>Illite</b>	20	100-2,000	80-120	10-40
<b>Chlorite</b>	30	100-2,000	70-90	10-40
<b>Kaolinite</b>	100	10-1,000	10-15	3-15

**Table 2:** Experimental data. TC = turbidity current. \* Froude number calculated with an  $H$  given by volume conservation (see Dimensional analysis of maximum head velocity and run-out distance).

Run number	Sediment type	Initial sediment concentration $C$ (vol %)	Run-out distance (m)	Maximum head velocity ( $\text{m s}^{-1}$ )	Froude Number * (-)	Yield stress ( $\text{N m}^{-2}$ )	Flow type
1	Silica flour	1	-	0.11	0.81	-	Low-density TC
2	Silica flour	5	-	0.24	0.90	-	Low-density TC
3	Silica flour	10	-	0.34	0.95	-	Low-density TC
4	Silica flour	15	-	0.45	0.68	-	Low-density TC
5	Silica flour	25	-	0.58	0.72	-	Low-density TC
6	Silica flour	40	-	0.69	0.76	-	Low-density TC
7	Silica flour	44	-	0.71	0.68	-	Low-density TC
8	Silica flour	46	-	0.75	0.81	-	High-density TC
9	Silica flour	47	4.66	0.75	0.71	-	High-density TC
10	Silica flour	48	3.68	0.71	0.64	-	High-density TC
11	Silica flour	49	2.82	0.71	0.66	-	High-density TC
12	Silica flour	50	1.53	0.64	0.57	-	High-density TC
13	Silica flour	51	0.96	0.61	0.49	-	Mud flow
14	Silica flour	52	0.49	0.29	0.20	-	Slide
15	Kaolinite	1	-	0.11	0.70	-	Low-density TC
16	Kaolinite	5	-	0.28	0.65	0.34	Low-density TC
17	Kaolinite	10	-	0.33	0.63	8.77	Low-density TC
18	Kaolinite	15	-	0.41	1.22	15.5	Low-density TC
19	Kaolinite	22	4.35	0.48	0.87	41.2	High-density TC
20	Kaolinite	23	3.66	0.48	0.66	-	High-density TC
21	Kaolinite	25	2.09	0.46	0.56	67.2	High-density TC
22	Kaolinite	27	1.01	0.40	0.37	93.8	Mud flow
23	Kaolinite	29	0.45	0.13	0.12	141.2	Slide
24	Bentonite	1	-	0.10	0.71	-	Low-density TC
25	Bentonite	5	-	0.23	0.92	0.77	Low-density TC
26	Bentonite	10	-	0.31	1.12	7.35	Low-density TC
27	Bentonite	15	4.66	0.35	0.56	21.7	High-density TC
28	Bentonite	16	3.77	0.37	1.20	28.9	High-density TC
29	Bentonite	17	3.12	0.35	0.96	34.7	High-density TC
30	Bentonite	18	1.42	0.27	0.53	37.0	Mud flow
31	Bentonite	19	1.22	0.25	0.42	119.0	Mud flow
32	Bentonite	20	0.22	0.05	0.06	217.3	Slide

**Table 3:** Summary of flow and deposit properties. Dimensional height is relative to the maximum thickness of the deposit. Dimensionless distance is relative to the run-out distance.

	Low-density turbidity current (LDTC)	High-density turbidity current (HDTC)	Cohesive and non-cohesive mud flow (CMF/NCMF)	Slide
<b>Visual flow properties</b>	Fully turbulent; uniform colour; mixing with ambient water	Dense lower layer and dilute upper layer; mixing with ambient water	Weak to no internal turbulence; some sediment entrained at top, producing dilute sediment cloud	Coherent mass without significant internal deformation
<b>Flow shape and internal structures</b>				
<b>Deposit shape</b>	Not measured, but probably elongate, thin and wedge-shaped (cf., Amy <i>et al.</i> , 2005)			
<b>Range of C-values</b>	Silica flour: $C \leq 44\%$ Kaolinite: $C \leq 15\%$ , Bentonite: $C \leq 10\%$	Silica flour: $46\% \leq C \leq 50\%$ Kaolinite: $22\% \leq C \leq 25\%$ Bentonite: $15\% \leq C \leq 17\%$	Silica flour: $C = 51\%$ Kaolinite: $C = 27\%$ Bentonite: $18\% \leq C \leq 19\%$	Silica flour: $C = 52\%$ Kaolinite: $C = 29\%$ Bentonite: $C = 20\%$
<b>Yield stress boundaries</b>	Lower boundary: $0 \text{ N m}^{-2}$ Upper boundary: $16\text{-}22 \text{ N m}^{-2}$	Lower boundary: $16\text{-}22 \text{ N m}^{-2}$ Upper boundary: $67\text{-}94 \text{ N m}^{-2}$	Lower boundary: $67\text{-}94 \text{ N m}^{-2}$ Upper boundary: $119\text{-}141 \text{ N m}^{-2}$	Lower boundary: $119\text{-}141 \text{ N m}^{-2}$ Upper boundary: $268 \text{ N m}^{-2}$